Mapping Curie temperature depth in the western United States with a fractal model for crustal magnetization

Claire Bouligand,[1,2] Jonathan M. G. Glen,[1] and Richard J. Blakely[1]

[1]   We have revisited the problem of mapping depth to the Curie temperature isotherm from magnetic anomalies in an attempt to provide a measure of crustal temperatures in the western United States. Such methods are based on the estimation of the depth to the bottom of magnetic sources, which is assumed to correspond to the temperature at which rocks lose their spontaneous magnetization. In this study, we test and apply a method based on the spectral analysis of magnetic anomalies. Early spectral analysis methods assumed that crustal magnetization is a completely uncorrelated function of position. Our method incorporates a more realistic representation where magnetization has a fractal distribution defined by three independent parameters: the depths to the top and bottom of magnetic sources and a fractal parameter related to the geology. The predictions of this model are compatible with radial power spectra obtained from aeromagnetic data in the western United States. Model parameters are mapped by estimating their value within a sliding window swept over the study area. The method works well on synthetic data sets when one of the three parameters is specified in advance. The application of this method to western United States magnetic compilations, assuming a constant fractal parameter, allowed us to detect robust long-wavelength variations in the depth to the bottom of magnetic sources. Depending on the geologic and geophysical context, these features may result from variations in depth to the Curie temperature isotherm, depth to the mantle, depth to the base of volcanic rocks, or geologic settings that affect the value of the fractal parameter. Depth to the bottom of magnetic sources shows several features correlated with prominent heat flow anomalies. It also shows some features absent in the map of heat flow. Independent geophysical and geologic data sets are examined to determine their origin, thereby providing new insights on the thermal and geologic crustal structure of the western United States.

1.   Introduction

[2]   The western United States, and in particular the Great Basin, is unique in its magmatic and tectonic history, having been affected by Basin and Range extension, Yellowstone hot spot magmatism, and a protracted history of subduction beneath the North American Plate. Great Basin heat flow is distinguished from surrounding areas (Figure 1). This highly extended area is characterized by high heat flow that contrasts with the prominent low heat flow observed over the adjacent Great Valley, Colorado Plateau, and Wyoming Basin (Figure 1). It also is distinct from very high heat flow regions over relatively young volcanic areas, notably the Cascade arc, a product of subduction of the Juan de Fuca Plate and the Snake River Plain, which marks the track of

the Yellowstone hot spot. Spatial variations of heat flow also can be distinguished within the Great Basin. *Sass et al.* [1971] recognized two main features, the Battle Mountain High and the Eureka Low heat flow areas. Recent heat flow maps (Figure 1) [*Blackwell and Richards*, 2004] also display these features, albeit with slightly different shapes.

[3]   However, heat flow in part of the western United States is still poorly constrained, due in part to the sparse and uneven distribution of data. Moreover, because of the high density of faults and the juxtaposition of basins and ranges in the Great Basin, many areas in this region are either affected by groundwater circulation or display strong contrasts in thermal conductivity that may render heat flow measurements unsuitable for characterizing trends in lower crustal heat flow [e.g., *Blackwell*, 1983]. Whereas the Battle Mountain High is believed to reflect true conductive heat flow variations possibly due to higher extension rates over this area [*Lachenbruch*, 1978], the Eureka Low is likely caused by regional hydrologic effects [e.g., *Sass et al.*, 1971; *Lachenbruch and Sass*, 1977]. Estimating heat flow in the Snake River Plain is also difficult because the region

---

[1]U.S. Geological Survey, Menlo Park, California, USA.
[2]Now at Laboratoire de Géophysique Interne et Tectonophysique, Université Joseph-Fourier, CNRS, Grenoble, France.
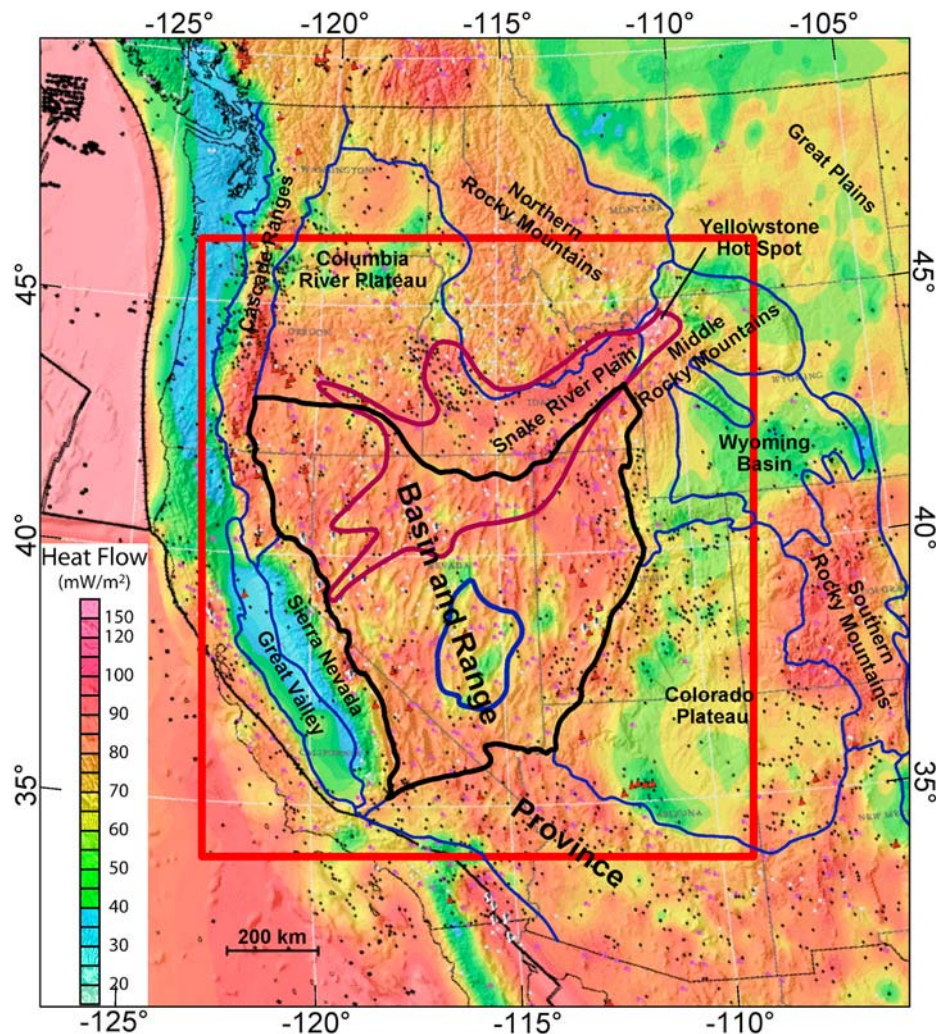
Figure 1. Map of the heat flow in the western United States, modified from *Blackwell and Richards* [2004]. Heat flow data are located by black dots. Also represented are physiographic provinces (blue outlines; modified from *Fenneman and Johnson* [1946]), the limit of the Great Basin (black outline), the Battle Mountain High heat flow area (thick maroon outline), and the Eureka Low heat flow area (thick blue outline) as defined by *Sass et al.* [1994]. The red square outlines our study area.

is marked by strong conductivity contrasts at the edges of the volcanic plain and an aquifer covers its eastern branch [e.g., *Blackwell*, 1989]. Independent estimates of crustal temperature would be helpful in assessing western United States heat flow and would aid understanding of the thermal history of the region, related to, for example, the initiation and early track of the Yellowstone hot spot, the extent of ancestral Cascade arc volcanism, the influence of Basin and Range extension in the Great Basin, and volcanism associated with a remnant Farallon slab.

[4] Several methods have been proposed to provide an independent assessment of crustal temperatures from magnetic anomalies. Such methods typically assume that the depth extent of crustal magnetic sources corresponds to the Curie temperature, the temperature at which rocks lose their spontaneous magnetization (e.g., ~580°C for magnetite). These methods usually operate in the Fourier domain by analyzing the shape of the power spectrum calculated from aeromagnetic anomalies [e.g., *Spector and Grant*, 1970],

and they critically depend on assumptions about the distribution of crustal magnetization [*Fedi et al.*, 1997; *Ravat et al.*, 2007]. Early methods assumed that crustal magnetization is a completely random function of position characterized by a flat power density spectrum [e.g., *Connard et al.*, 1983; *Blakely*, 1988; *Tanaka et al.*, 1999; *Ross et al.*, 2006]. However, other studies have suggested that crustal magnetization more closely follows fractal behavior [e.g., *Pilkington et al.*, 1994; *Maus and Dimri*, 1995, 1996; *Lovejoy et al.*, 2001; *Pecknold et al.*, 2001; *Gettings*, 2005]. The method used in the present study is derived from a method initially developed by *Maus et al.* [1997] that incorporates a model of fractal random magnetization, thus providing a more realistic representation for crustal magnetization. The power spectrum of magnetization is assumed to be proportional to the wave number raised to a power $-\beta$. The radial average of the power spectrum (referred to as "radial power spectrum" in this paper), as derived by *Maus et al.* [1997], is complex but in fact depends on only three independent

parameters: the depths to the top and bottom of the magnetic source layer and the fractal exponent β. We show that the theoretical expression of *Maus et al.* [1997] that includes an integral term can be resolved analytically. Model parameters are estimated by fitting this theoretical curve to the calculated radial power spectrum obtained from the magnetic anomaly map. We first tested this methodology on synthetic aeromagnetic data and then applied it to newly released aeromagnetic compilations for Nevada [*Kucks et al.*, 2006] and the western United States [*North American Magnetic Anomaly Group* (*NAMAG*), 2002]. In our application, the magnetic anomaly map is broken into overlapping windows. Each window is analyzed for a single depth, thereby providing a regional-scale view of the depth to the bottom of magnetic sources across the entire magnetic anomaly map.

2. Data

[5] Deep magnetic sources mainly affect the longer wavelengths of the crustal magnetic field. Thus, estimation of the depth to the bottom of magnetic sources requires magnetic anomaly data covering very broad areas. No single aeromagnetic survey covers the entire western United States and we are restricted to using compilations derived from numerous regional surveys. In this study, we use two such compilations: the magnetic anomaly map of North America [*NAMAG*, 2002] and the state map of Nevada [*Kucks et al.*, 2006]. The Nevada compilation includes several newer surveys and has been gridded at a finer interval than the North America compilation (0.5 km for Nevada and 1 km for North America). These two grids consist of total field anomalies obtained after removal of the intensity of the main magnetic field. They were compiled from surveys that were upward or downward continued to the same elevation of 305 m above the ground. Because these compilations include many different aeromagnetic surveys characterized by different specifications, such as flight elevation, flight line spacing, and IGRF model, they may display artifacts, such as offsets or changes in spectral content across the survey boundaries. It is essential to consider these factors when analyzing and interpreting the data.

[6] To limit long-wavelength artifacts due to offsets between individual surveys, lithospheric magnetic models from CHAMP satellite data were also used in these compilations. In particular, individual surveys in the Nevada compilation were adjusted by adding or removing a constant to fit the magnetic field predicted at flight elevation by model MF4x [*Lesur and Maus*, 2006]. A simpler approach was used for the North America compilation, where long wavelengths (above 500 km) were removed from the initial merged grid and replaced by the magnetic field predicted by model MF1 [*Maus et al.*, 2002]. In our study, this later correction in the North America compilation has little effect since we estimated power spectra over computational windows with a maximum size of 300 km. Power spectra obtained from initial and corrected grids display minor differences that do not affect our results. For this reason, we simply used the initial merged grid obtained for the North America compilation that does not include a satellite data correction for the long wavelengths. Also, since short wavelengths (below ~500 km) are poorly constrained by

satellite data, correction or adjustment of aeromagnetic data with satellite data are likely not perfect. As a consequence, wavelengths larger than the size of individual surveys (about 200 km) are relatively poorly constrained in these compilations.

3. Methodology
3.1. Assumptions

[7] We estimate the depth to the bottom of magnetic sources by analyzing the Fourier spectrum of total field magnetic anomalies while assuming a model of fractal random crustal magnetization, as proposed by *Maus et al.* [1997]. Anomalies are assumed to be measured on a horizontal plane at an elevation z_t above magnetic sources. Magnetic sources are assumed to reside within a horizontal slab of thickness Δz, with magnetization oriented parallel or antiparallel to the geomagnetic field. Magnetization is assumed to be a random function of position (x, y, z), with a power spectrum proportional to the norm of the wave number raised to power $-\beta$:

$$\Phi_M(k_x, k_y, k_z) \propto k^{-\beta} \tag{1}$$

where $\Phi_M(k_x, k_y, k_z)$ is the 3-D power spectrum of magnetization, $\vec{k} = (k_x, k_y, k_z)$ is the wave number, and $k = |\vec{k}| = 2\pi/\lambda$ is its norm, where λ is the wavelength. The fractal parameter β, which is the slope of the power spectrum in a log-log scale, is related to the geology and thus might vary geographically depending on rock types or geologic structures. With these assumptions, the magnetic sources can be fully described by three unknowns: the depth to the top of magnetic sources z_t, the thickness of magnetic sources Δz, and the fractal parameter β.

[8] To solve this problem, *Maus et al.* [1997] proposed computing the radial average of the logarithm of the power spectrum of magnetic anomalies, instead of the logarithm of the radial average commonly adopted by previous studies:

$$\Phi_{B1D}(k_H) = \int_0^{2\pi} \ln\left[\Phi_{B2D}(k_x, k_y)\right] d\theta \tag{2}$$

where $\Phi_{B1D}(k_H)$ and $\Phi_{B2D}(k_x, k_y)$ are the radial power spectrum and the 2-D power spectrum of magnetic anomalies, respectively, $\vec{k}_H = (k_x, k_y)$ is the wave number in the horizontal plane, $k_H = |\vec{k}_H|$ is its norm, and θ is its angle with respect to k_x. This definition leads to an analytic expression for the radial power spectrum, with a shape that depends only on the three unknowns, z_t, Δz, and β [*Maus et al.*, 1997]:

$$\Phi_{B1D}(k_H) = C - 2k_H z_t - k_H \Delta z - \beta \ln(k_H)$$
$$+ \ln\left[\int_0^\infty (\cosh(k_H \Delta z) - \cos(k_z \Delta z))\left(1 + \left(\frac{k_z}{k_H}\right)^2\right)^{-1-\frac{\beta}{2}} dk_z\right] \tag{3}$$

where C is a constant. The orientation of the geomagnetic field appears only in the constant C [*Maus et al.*, 1997]. Thus, the shape of the radial power spectrum is independent of the direction of the geomagnetic field. We show in Appendix A
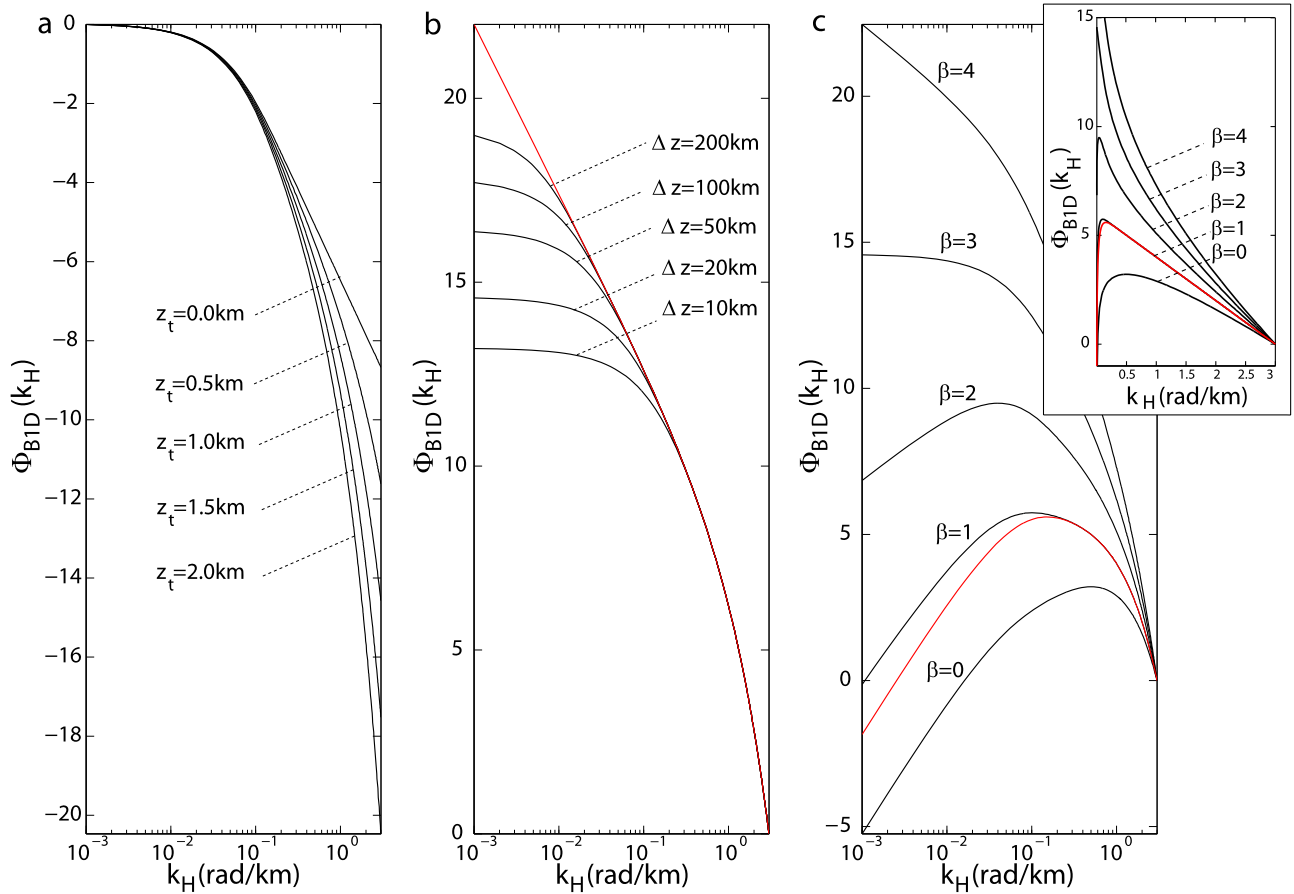
Figure 2. Theoretical radial power spectra (black curves) of magnetic anomalies $\Phi_{B1D}(k_H)$ defined by expression (4) and predicted for different values of the (a) depth to the top z_t, (b) thickness Δz, and (c) fractal parameter β of magnetic sources. Values of the two other fixed parameters are $z_t = 1$ km, $\Delta z = 20$ km, $\beta = 3$. The horizontal scale has been set to a logarithmic scale in order to highlight the long-wavelength part of the power spectrum. The plot on the top right corner of Figure 2c shows the shape of theoretical radial power spectra for a linear horizontal scale. The red curve in Figure 2b is the theoretical radial power spectrum predicted for a half-space as defined by expression (5). The red curve in Figure 2c is the theoretical radial power spectrum defined by expression (9) and used by early studies [e.g., *Connard et al.*, 1983; *Okubo et al.*, 1985; *Blakely*, 1988; *Tanaka et al.*, 1999; *Ross et al.*, 2006].

that the integral in expression (3) can be resolved analytically, which leads to the following expression:

$$\Phi_{B1D}(k_H) = C - 2k_H z_t - (\beta - 1)\ln(k_H)$$
$$+ \left[-k_H \Delta z + \ln\left(\frac{\sqrt{\pi}}{\Gamma\left(1 + \frac{\beta}{2}\right)} \left(\frac{\cosh(k_H \Delta z)}{2} \Gamma\left(\frac{1+\beta}{2} \right) \right.\right.$$
$$\left.\left. - K_{\frac{1+\beta}{2}}(k_H \Delta z)\left(\frac{k_H \Delta z}{2} \right)^{\frac{1+\beta}{2}} \right) \right) \right]$$

(4)

where $\Gamma(u)$ is the gamma function and $K_\alpha(u)$ is the modified Bessel function of the second kind.

[9] The final term in brackets in equation (4) vanishes as Δz becomes large, so that the radial power spectrum for a half-space of magnetic sources is given by [*Maus and Dimri*, 1995]

$$\Phi_{B1D}(k_H) = C - 2k_H z_t - (\beta - 1)\ln(k_H)$$

(5)

Thus, the effect of finite Δz is contained entirely in the final bracketed term of equation (4). This term, which depends on Δz and β, significantly influences the shape of the radial power spectrum at low wave numbers (Figure 2b). The radial power spectrum of a finite layer is similar to those of a half-space at high wave numbers, but diverges from this curve at low wave numbers. This divergence occurs at lower wave numbers, as the layer thickness increases. This reveals that the deeper the bottom of magnetic sources, the larger the window will need to be in order to recover low wave numbers in the radial power spectrum and to accurately estimate the depth to the bottom of magnetic sources. In contrast, the depth to the top of magnetic sources z_t influences the slope of the radial power spectrum at high wave numbers (Figure 2a). Specifically, the slope of the spectrum at high wave numbers increases with increasing z_t. Finally, the fractal parameter β influences the general shape of the radial power spectrum over the whole range of wave numbers. The radial power spectrum displays a peak for small β (≤ 2) but not for large β (≥ 3) (Figure 2c). As β increases, the slope of the radial power spectrum at high

wave numbers increases, and the difference in slope between low and high wave numbers decreases.

[10] It is clear from Figure 2 that the influence of β overlaps the range of wave numbers influenced by z_t and Δz. Thus, it is not possible to derive a simple analytic method to recover all three parameters (z_t, Δz, β) from equation (4). Instead we estimate the unknown parameters by fitting theoretical curves to the radial power spectrum of magnetic anomalies. The depth to the bottom of magnetic sources z_b is simply deduced from the depth to the top z_t and the thickness Δz, $z_b = z_t + \Delta z$.

3.2. Application

[11] In order to obtain a map of the depth to the bottom of magnetic sources, radial power spectra of magnetic anomalies were computed within overlapping rectangular windows regularly spaced over the aeromagnetic map (Figure 3a). For each window, we first computed 2-D Fourier power spectra of the magnetic field $\Phi_{B2D}(k_x, k_y)$ for discrete wave numbers, k_x and k_y ranging from $2\pi/W$ to $\pi/\Delta l$, W being the window size and Δl the sampling interval of the aeromagnetic grid. We then estimated the radial power spectrum $\Phi_{B1D}(k_H)$ within each window, as defined in (2), by averaging $\Phi_{B2D}(k_x, k_y)$ in rings of width $2\pi/W$ concentric about the origin. For each mean value, we also computed a 95% confidence interval α_{95} that gives an estimate of the uncertainty in the radial power spectrum:

$$\alpha_{95} = 1.96 \frac{\sigma}{\sqrt{N}} \qquad (6)$$

where σ is the standard deviation evaluated in the ring and N is the number of values contained in the ring. Examples of radial power spectra are shown in Figure 3. Larger α_{95} confidence intervals occur at low wave numbers because low wave number rings have fewer values in the average, reflecting the fact that radial power spectra are less constrained at long wavelengths.

[12] Finally, the unknown parameters z_t, Δz, and β were evaluated by searching for values that lead to a minimum misfit between the theoretical curve $\Phi_{B1D\ \mathrm{th}}(k_H)$ expressed in (4) and the calculated radial power spectrum $\Phi_{B1D\ \mathrm{calc}}(k_H)$. The misfit R is defined as

$$R = \sqrt{\frac{1}{N} \sum_{k_H} \left(\Phi_{B1D\ \mathrm{calc}}(k_H) - \Phi_{B1D\ \mathrm{th}}(k_H) \right)^2} \qquad (7)$$

where N is the number of points in the calculated radial power spectrum. The value of minimum misfit gives a quantitative measure of the fit between theoretical and calculated radial power spectra. In practice, the fit is performed automatically using the lsqcurvefit tool from MATLAB® that solves nonlinear curve-fitting problems in the least squares sense. The algorithm used in this function starts from initial parameter values and quickly converges through several iterations to the best fit solution using the partial derivatives of the theoretical expression in (4) with respect to the unknown parameters.

[13] Figure 3b shows two radial power spectra calculated for the same window over the Nevada and the North American aeromagnetic maps (see Figure 3a for location).
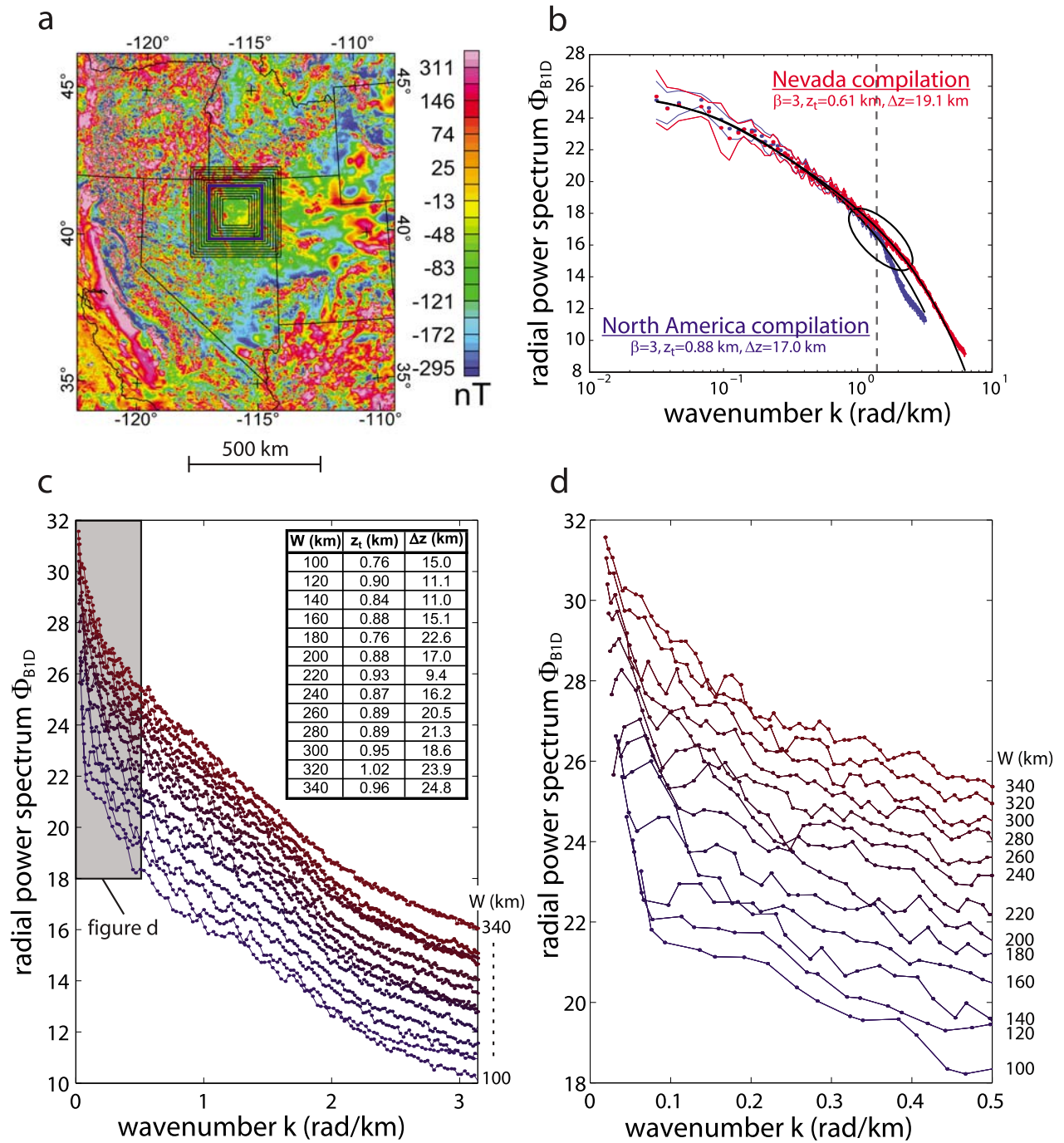
These two spectra are very similar at low wave numbers but diverge at high wave numbers. Divergence occurs at wave numbers higher than ~1.4 rad/km in this example, but this threshold varies over the study area. At high wave numbers, both spectra diverge from the theoretical shape predicted by *Maus et al.* [1997]. This divergence, probably due to noise or aliasing, is observed at lower wave numbers for the North America compilation than for the Nevada compilation. For this reason, we restricted the range of wave numbers, used for depth calculations, to wave numbers lower than 3 rad/km for the Nevada compilation and 2 rad/km for the North America compilation. Note that we did not use smaller values, such as 1.4 rad/km for the North American compilation as tests indicated that smaller values yielded similar depths but noisier results.

3.3. Limits and Resolution

[14] In this section, we address the uniqueness and accuracy of estimating the three parameters z_t, Δz and β. To this end, we first applied the fitting method to a radial power spectrum calculated according to equation (4). For example, applying the fitting method to a theoretical curve calculated for discrete wave numbers between 0.03 and 2 rad/km and with $z_t = 0.305$ km, $\Delta z = 10$ km, and $\beta = 3$ leads to a very accurate solution ($z_t = 0.318$ km, $\Delta z = 10.34$ km, $\beta = 2.97$) and a very small misfit of 0.003. However, if we intentionally set a wrong value to one of the parameters, for example $\beta = 4$, the fitting method leads to an erroneous answer for the other parameters (in this case $z_t = -0.046$ km, $\Delta z = 2.94$ km) with a larger but still very small misfit of 0.082. Although the fit is better for the correct answer, it might be difficult to distinguish these two cases when dealing with real radial power spectra obtained from aeromagnetic data with inevitable noise.

[15] For this reason, the methodology was also tested on synthetic data sets computed using a model of fractal random magnetization following a method proposed by *Pilkington and Todoeschuck* [1993]. The synthetic data sets were constructed in the following way. We first filled a cubic grid composed of $305 \times 305 \times 305$ cells. Each cell was a 1 km cube and was assigned a random value of magnetization drawn from a Gaussian distribution with a mean value of 0 A/m and a standard deviation of 0.2 A/m. The mean value was set to 0 A/m, but this value is irrelevant because a slab of constant magnetization produces no magnetic field. The volume of fractal random magnetization was obtained by computing the 3-D Fourier transform of this volume, multiplying it by the norm of the wave number at a power $-\beta/2$ and then computing its inverse Fourier transform. We then calculated the magnetic anomaly at an elevation z_t above a slab of thickness Δz extracted from this cubic volume. To this end, we summed the anomaly contribution due to each layer of cells within the slab, obtained by computing their 2-D Fourier transform, multiplying them by the Earth filter (as in the expression (11.35) of *Blakely* [1995]) and computing their inverse Fourier transform. For simplification, the direction of magnetization and geomagnetic field were assumed to be vertical. Figure 4a displays an example with layer thickness $\Delta z = 10$ km and fractal parameter $\beta = 3$. Because $\beta > 0$, this model of magnetization is not completely random but rather displays long-wavelength patterns reminiscent of crustal magnetiza-

W (km)	z_t (km)	Δz (km)
100	0.76	15.0
120	0.90	11.1
140	0.84	11.0
160	0.88	15.1
180	0.76	22.6
200	0.88	17.0
220	0.93	9.4
240	0.87	16.2
260	0.89	20.5
280	0.89	21.3
300	0.95	18.6
320	1.02	23.9
340	0.96	24.8

Figure 3. (a) Portion of the aeromagnetic compilation of North America. The black squares indicate the limits of the windows used to compute the radial power spectra presented in Figures 3c and 3d. The bold blue square represents the limits of the window used to compute the radial power spectra presented in Figure 3b. (b) Radial power spectra calculated from Nevada (red) and North America compilations (blue), with a window size of 200 km. The dots and the thin solid colored lines represent the radial power spectrum and the 95% confidence interval α_{95}, respectively. The bold black curves are theoretical curves for a model of fractal random magnetization that best fit the calculated power spectrum, assuming a fractal parameter $\beta = 3$. Results of these fits, depth to the top z_t, and thickness of magnetic layer Δz, are indicated on the top for the Nevada compilation and on the bottom for the North America compilation. These fits were performed using wave numbers ranging from 0 to 3 rad/km for the Nevada compilation and 0 to 1.4 rad/km for the North America compilation. (c) Radial power spectra calculated from the North America compilation for different window sizes, from 100 km (in red) to 340 km (in blue). The table, in the top right corner, shows the results of the fit, performed using wave numbers between 0 and 1.4 rad/km as a function of the size of the window. (d) Expanded portion of Figure 3c represented by the gray square showing the long-wavelength (low wave number) part of the spectra.

tion, where large crustal features, such as plutons, contrast with surrounding basement. The map of magnetic anomalies computed at an elevation $z_t = 0.305$ km above the magnetic layer (same elevation as the flight elevation in the aeromagnetic compilations used in this study) displays realistic anomaly amplitudes of about ±300 nT (Figure 4b).
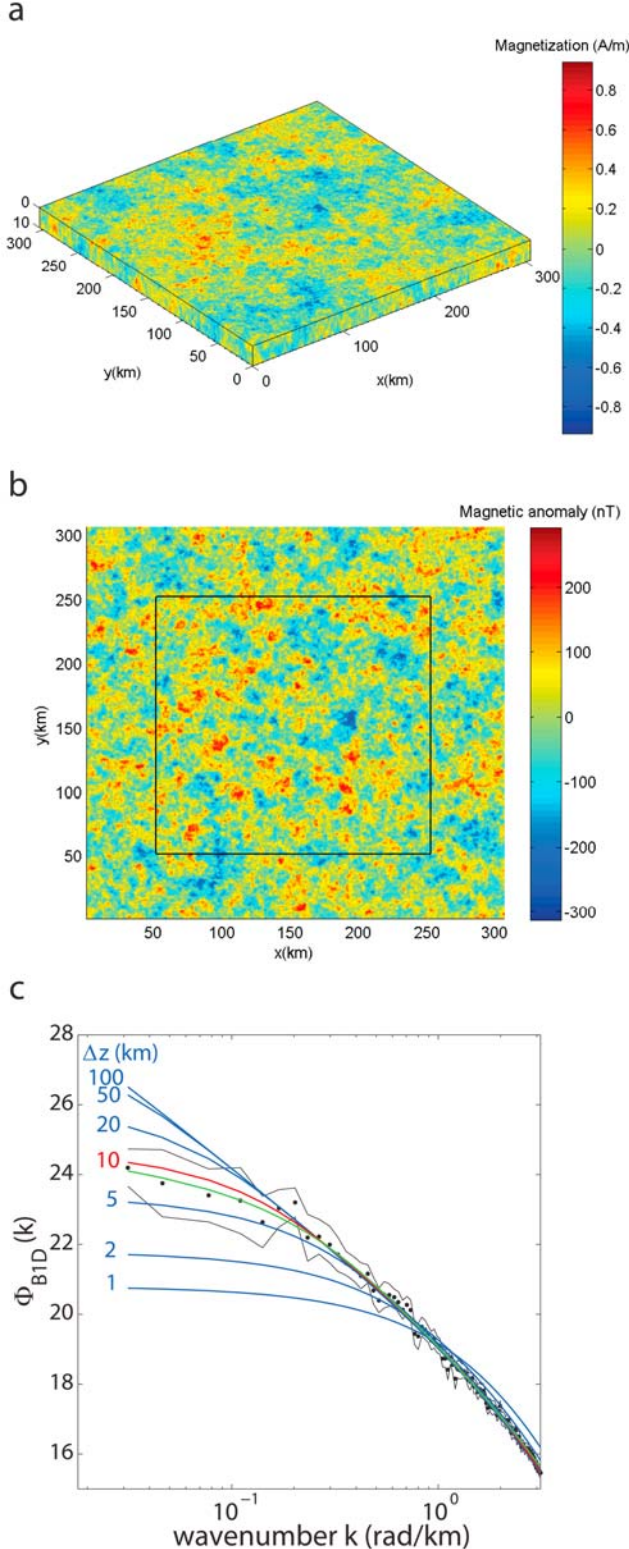

[16] Figure 4c displays the radial power spectrum computed in a window of $(200 \text{ km})^2$ over this synthetic anomaly map. The theoretical curve corresponding to the actual parameters used to create the synthetic data lies within the 95% confidence interval, as it should. However, other curves obtained for different values of the three parameters are also consistent with the data (for instance $\Delta z = 5$ km), showing that the resolution of the method is limited. Indeed, using nonlinear least squares to determine all three parameters simultaneously leads to the following erroneous parameters: $z_t = 0.203$ km, $\Delta z = 5.93$ km, $\beta = 3.26$ with a misfit of 0.174. However, if we assume that we know the correct value of one of the three parameters, we obtain slightly better estimates of the remaining two parameters. For example, assuming $\beta = 3$ leads to $z_t = 0.320$ km and $\Delta z = 7.99$ km, with a misfit of 0.177; assuming $z_t = 0.305$ km leads to $\Delta z = 7.46$ km and $\beta = 2.86$ with a misfit of 0.176; and finally, assuming $\Delta z = 10$ km leads to $z_t = 0.380$ and $\beta = 2.86$ with a misfit of 0.182. This example shows that, in practice, the solution is not unique and fitting the radial power spectrum by estimating all three unknown parameters simultaneously can lead to erroneous results.

[17] In order to determine the origin of the nonuniqueness, we evaluated the value of the misfit between the radial power spectrum obtained from the synthetic data and a variety of theoretical power spectra obtained for a range of values of the unknown parameters. Figure 5 displays the matrix of the misfits obtained when we vary two of the parameters while holding the third parameter to its correct value. The three plots in Figure 5 display a prominent minimum, showing that in practice the fitting method will give a unique although not necessarily accurate solution. Moreover, the shape of the contour lines around these minima is not circular, indicating that errors on the estimation of one parameter can be compensated by errors on the

Figure 4. (a) Slab of fractal random magnetization composed of $305 \times 305 \times 10$ cells of $(1 \text{ km})^3$ computed assuming a fractal parameter $\beta = 3$ and a mean value and standard deviation of the magnetization of 0 ± 0.2 A/m. (b) Resulting synthetic map of magnetic anomalies computed at an elevation of 305 m above the layer of fractal random magnetization. (c) Radial power spectrum (black dots) computed from the map of magnetic anomalies in b using a window of 200×200 km^2 whose limits are represented by the black square plotted in Figure 4b. The black lines represent the bound of the 95% confidence interval for the radial power spectrum. The blue curves give the theoretical power spectrum predicted for a layer of fractal random magnetization with a depth to the top $z_t = 0.305$ km, a fractal parameter $\beta = 3$, and a thickness $\Delta z = 1$, 2, 5, 20, 50, or 100 km. The red curve is the theoretical power spectrum predicted for the actual parameters used to create the synthetic anomaly map ($z_t = 0.305$ km, $\beta = 3$, $\Delta z = 10$ km). The green curve is the theoretical curve that best fits the synthetic radial power spectrum ($z_t = 0.203$ km, $\beta = 3.26$, $\Delta z = 5.93$ km). Note that although the theoretical power spectrum predicted for the actual parameters (in red) is consistent with the synthetic radial power spectrum (within the 95% confidence interval), fitting all three parameters simultaneously leads to erroneous results.

estimation of the other parameters. For instance, the elongated shape of the contour lines in the (β, z_t) space (Figure 5a) indicates that a larger fractal parameter β can be compensated by a smaller depth to the top, z_t. This reflects that both
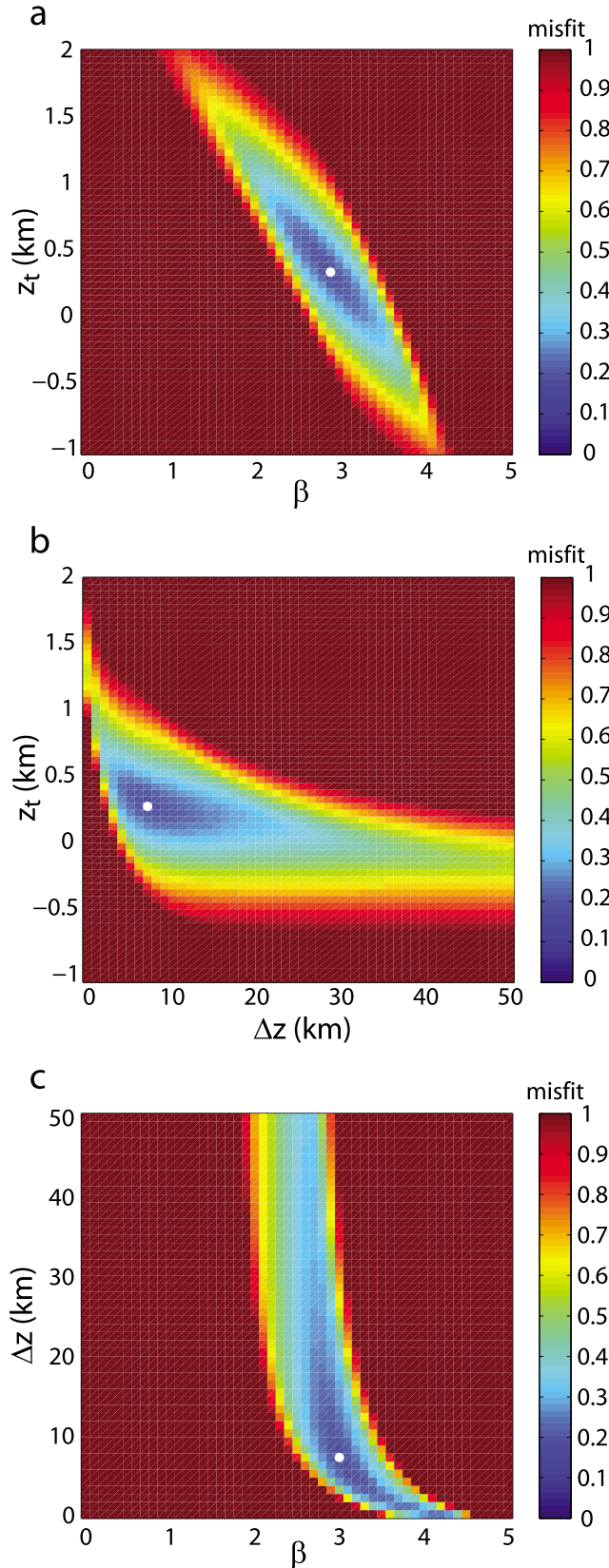

parameters have relatively similar effects at high wave numbers, where the radial power spectrum is better constrained. The more complex shape of the contour lines in Figures 5b and 5c indicates first that a smaller thickness Δz can be compensated by a larger fractal parameter β or by a larger depth to the top z_t, and second that the value of Δz is much less constrained than the values of β and z_t. Indeed, a small misfit (e.g., less than 0.3) is obtained for larger ranges of Δz than for z_t or β.

[18] In order to further investigate uncertainties on estimated parameters, we produced 100 unique synthetic anomaly maps, each with a separate realization of random magnetization, and applied the same fitting method to each. Figure 6 (black dots) shows results obtained using a window size of 200 km with all three parameters estimated simultaneously. The estimated values for the parameters are distributed within a broad cloud of points around the correct values. Figures 6a and 6c show that in rare cases, unrealistically high values are obtained for Δz. This may simply reflect the difficulty in distinguishing between the shape of radial power spectra obtained for a thick layer and for a half-space (see Figure 4c). Figure 6 also shows correlations between errors on the different parameters, confirming the conclusions drawn above from the description of the misfit matrix (Figure 5).

[19] We repeated the experiment for different window sizes and also by setting one of the parameters to its actual value. In order to compare the dispersion of the results around the correct answer, we computed for each type of experiment the median of the relative error, i.e., the median of the absolute errors obtained for the 100 model runs divided by the correct value of the parameters (Figure 7). We calculated the median rather than mean because in rare cases the fit led to erroneously high Δz that bias the statistics. Figure 7 shows that the relative error on Δz is much larger than the relative error on z_t or on β, which is again consistent with the conclusions drawn above from the description of the misfit matrix (Figure 5). As expected, the error generally decreases when the size of the window increases, reflecting that solutions are better constrained when a larger range of wave numbers is used for the fit. Setting the fractal parameter β or the depth z_t to their correct value leads to results distributed within a narrower cloud of points (Figures 6a and 6c) and to a significant decrease in the error on the estimate of the unknown parameters

Figure 5. Matrices of misfit calculated between the synthetic radial power spectrum plotted in Figure 4c and theoretical power spectra calculated for (a) the actual value of the thickness $\Delta z = 10$ km used to create the synthetic data and different values of the other unknowns β and z_t, (b) the actual value of the fractal parameter $\beta = 3$ and different values of Δz and z_t, and (c) the actual value of the depth to the top $z_t = 0.305$ km and different values of β and Δz. The white spots indicate the parameters that provide the minimum misfit within the range of parameters represented in Figures 5a–5c. These three plots show a prominent low with non circular contour lines indicating that although the best fit solution is unique, it is not necessarily accurate and that errors on the different parameters can compensate each others.
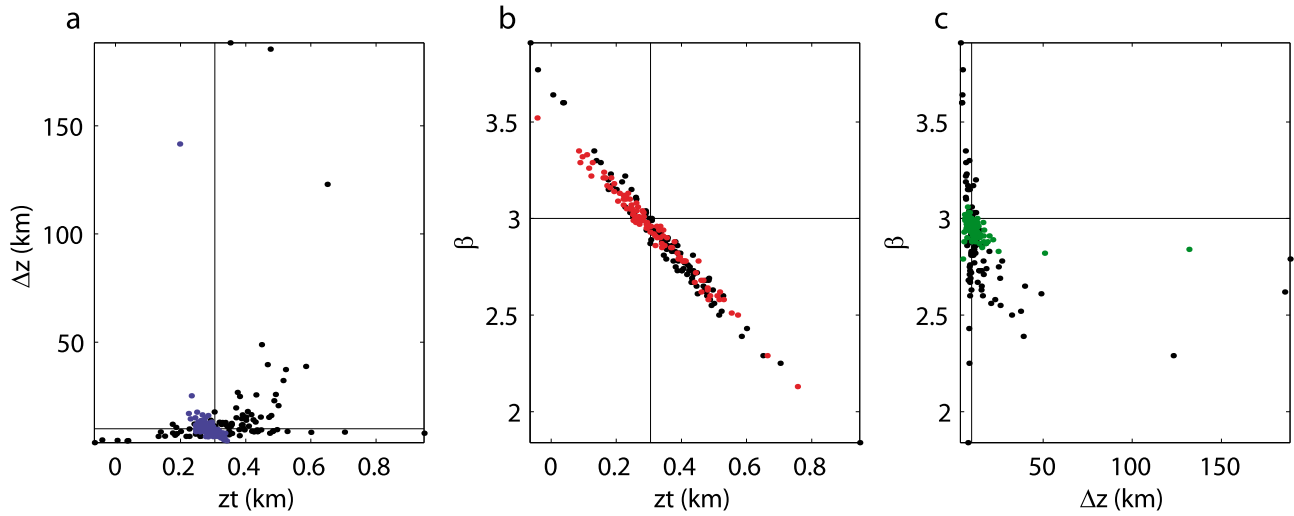
Figure 6. Results of the fitting method applied to radial power spectra calculated from 100 synthetic anomaly maps (calculated with the following parameters: $\beta = 3$, $z_t = 0.305$ km, $\Delta z = 10$ km) within a window of 200×200 km^2: (a) values of Δz versus z_t, (b) values of β versus z_t, and (c) values of β versus Δz. Results were obtained with none (in black) or one of the parameters a priori fixed (with β fixed in blue, Δz fixed in red, and z_t fixed in green). The horizontal and vertical lines on these graphs show the actual values of the parameters used to create the synthetic data. These three plots show that setting z_t or β to their correct value significantly decreases errors on the estimation of the two other parameters. On the other hand, setting Δz to its correct value does not significantly modify errors on the estimation of z_t or β.
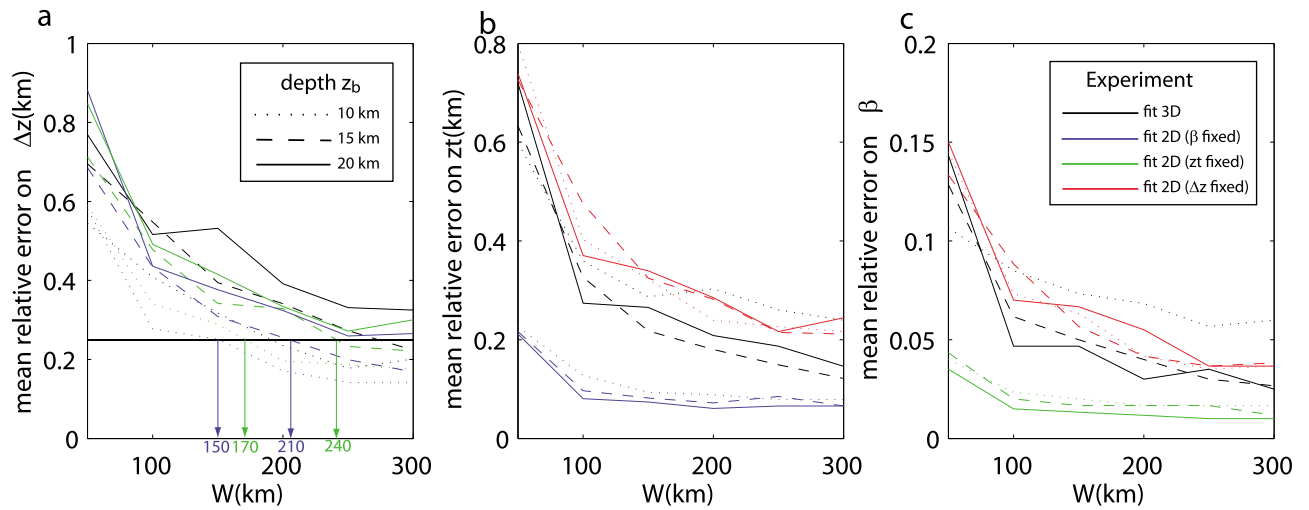
Figure 7. Median of the relative error on (a) Δz, (b) z_t, and (c) β obtained by applying the fitting method to radial power spectra calculated from 100 synthetic anomaly maps as a function of the window size W. The synthetic anomaly maps were created with the following parameters: $\beta = 3$, $z_t = 0.305$ km, and $\Delta z = 10$ km (dotted lines), $\Delta z = 15$ km (dashed lines) and $\Delta z = 20$ km (solid lines). Results obtained with none of the parameters a priori fixed are shown in black. Results obtained with the fractal parameter set to the correct value ($\beta = 3$) are shown in blue. Results obtained with the depth to the layer top set to the correct value ($z_t = 0.305$ km) are shown in green. Results obtained with the layer thickness set to the correct value ($\Delta z = 10$, 15, or 20 km) are shown in red. The horizontal black line in Figure 7a indicates a relative error of 25%. Errors on the estimation of the parameters generally decrease when z_t or β are set to their correct value or when the window size W increases. Setting z_t or β to their correct value leads to a median of the relative error on Δz of 25% for $W = 150–170$ km if $\Delta z = 10$ km and for $W = 210–240$ km if $\Delta z = 15$ km.

(Figures 7b and 7c). On the other hand, setting the correct value for Δz does not modify significantly the shape of the cloud of points (Figure 6b) and does not decrease the error on the estimate of β and z_t (Figure 7a), reflecting that uncertainties on the estimate of these two parameters are principally due to the nonuniqueness associated with the pair β and z_t. Finally, we repeated these experiments for models constructed with different layer thicknesses Δz (10 km, 15 km, 20 km). Figure 7a shows that for the same window size, the error on the estimate of Δz decreases as the true layer thickness decreases. Thus, our results, will be more reliable in places where z_b is expected to be shallow, as in regions of high heat flow. Setting the correct values for β or z_t and fitting the theoretical curve to the calculated radial power spectrum leads to a median of the relative error on the thickness Δz of 25% for a window size of about 160 km if $\Delta z = 10$ km, and of about 225 km if $\Delta z = 15$ km. We therefore conclude that the window size should be about 10–15 times larger than the depth extent of magnetic sources in order to obtain a well-constrained estimate of this parameter.

[20] It is important to keep in mind that the accuracy of the parameter estimation is likely lower for real data than for synthetic data sets because the fundamental assumptions of the methodology are only an approximation of the complexity of crustal magnetization. Note however that such an approximation seems to be appropriate as the theoretical curve expressed in (4) reproduces very well the shape of the radial power spectrum calculated from aeromagnetic anomalies (Figure 3b).

3.4. Comparison With Previous Studies

[21] Early studies have attempted to assess the depth to the bottom of magnetic sources by analyzing the shape of the Fourier radial power spectrum of aeromagnetic anomalies [e.g., *Connard et al.*, 1983; *Okubo et al.*, 1985; *Blakely*, 1988; *Tanaka et al.*, 1999; *Ross et al.*, 2006]. Those studies assumed that crustal magnetization is a random function of position and characterized by a flat power spectrum ($\beta = 0$). The power spectrum of magnetic anomalies, in this case, takes the following form:

$$\Phi_{B2D}(k_x, k_y) = C'[\exp(-k_H z_t) - \exp(-k_H(z_t + \Delta z))]^2 \quad (8)$$

leading to a radial power spectrum, as defined in (2), of the following form:

$$\Phi_{B1D}(k_H) = C'' - 2k_H z_t + 2\ln[1 - \exp(-k_H \Delta z)] \quad (9)$$

where C' and C'' are constants. This curve, represented in Figure 2c, lies close to the curve predicted by *Maus et al.* [1997] for a fractal magnetization of $\beta = 1$, instead of $\beta = 0$, as one might expect. This apparent contradiction is due to the fact that the magnetization model proposed by *Maus et al.* [1997] relies on slightly different assumptions than those generally assumed by earlier methods. *Maus et al.* [1997] assumed a random distribution of magnetization in three directions (x, y, z), whereas earlier methods only assumed a random distribution in horizontal directions (x, y) and a constant magnetization in the vertical direction.

[22] The shape of the radial power spectrum as calculated in previous studies ideally displays a peak at low wave

numbers. The estimation of the depth to the bottom of magnetic sources is performed by fitting the theoretical curves (9) to the calculated radial power spectrum. In practice, several methods have been used to perform this fit. *Connard et al.* [1983] used the slope of the power spectrum at high wave numbers to recover the depth to the top of magnetic sources z_t and then the position of the peak to recover the depth to the bottom of magnetic sources z_b. *Okubo et al.* [1985] and *Tanaka et al.* [1999] estimated the depth to the top and the depth to the "centroid" of magnetic sources by evaluating the slopes of the high wave number part of the radial power spectrum, and of the low wave number part of the radial power spectrum divided by the wave number, respectively. Finally, *Ross et al.* [2006] used a visual fit of the theoretical curve to the low wave number part of the radial power spectrum displaying a peak. The main drawback of all these methods is that the peak observed at low wave numbers, whose position is critical in the estimation of the depth to the bottom of magnetic sources, is often not observed or is only constrained by a few points in the radial power spectrum. As a result, the estimate of the depth to the bottom of magnetic sources, when it is even possible (i.e., when a peak is observed), is poorly constrained using these methods. The absence of a peak may simply indicate that the peak lies at wave numbers lower than the minimum resolved wave number and that a larger window size is needed to compute the radial power spectrum. On the other hand, the absence of a peak at low wave numbers may indicate fractal behavior of the magnetization. In order to test this latter explanation, we computed radial power spectra of aeromagnetic anomalies for windows centered on the same position with a range of increasing sizes (Figures 3a, 3c, and 3d). Doing so revealed that a peak is observed for some window sizes, but this peak shifts and eventually disappears with increasing window sizes. We further tried to estimate the depth to the bottom of magnetic sources by fitting the theoretical curve expressed in (9) to the low wave number part of the radial power spectrum, following *Ross et al.* [2006] but using the automated nonlinear least squares curve-fitting tool from MATLAB®. The results were strongly dependent on the window size, and, in some cases, Δz was out of realistic bounds because the shape of the peak did not match the shape predicted by expression (9). The strong dependence on the window size could be explained by spatial variations of the crustal magnetic thickness that are included when the window size is increased. More likely, the dependence indicates that observed peaks in this example are simply artifacts due to the finite size of the computational window. These observations show that expression (9) corresponding to a flat power spectrum of crustal magnetization (or approximated by a fractal parameter $\beta = 1$), as assumed by previous studies, is inappropriate in this particular example, although this might not be the case in all regions. On the other hand, our method, based on a fractal magnetization with a parameter $\beta > 1$, yields theoretical power spectra expressed in (4) that closely resemble the shape of observed power spectra over a much wider range of wave numbers (Figure 3b) and gives relatively stable results when the size of the window is increased (Figure 3c).

[23] Several previous studies have demonstrated fractal behavior of crustal magnetization based on spectral analysis

Table 1. Summary of Published Estimates for the Fractal Parameter β Within Various Contexts and From Spectral Analysis of Borehole Magnetic Susceptibility Profiles, Maps of Magnetic Susceptibility Measurements, and Aeromagnetic Maps[a]

β	Lithology	Location	Scale	Reference
		Borehole Magnetic Susceptibility Data		
2.4[b]	Metamorphic (gneiss, metabasite)	Bohemian Massif, Germany	20 m–1 km	*Maus and Dimri* [1995]
2.3–3.4[b]	Metamorphic (gneiss, metabasite)	Bohemian Massif, Germany	3 m–40 m	*Leonardi and Kümpel* [1996]
3.1–3.2[b]	Igneous (granodiorite, dacite)	Absaroka Mountain, United States	6 m–300 m	*Gettings* [2005]
3.32–3.96[b]	Sedimentary (sandstone, dolomite)	Ontario, Canadian shield	10 cm–10 m	*Pilkington and Todoeschuck* [1993]
4.08–4.72[b]	Igneous (granite, gneiss)	Ontario, Canadian shield	10 cm–10 m	*Pilkington and Todoeschuck* [1993]
		Mapping of Magnetic Susceptibility Measurements		
4[c]	Intrusive	Sierra Nevada, United States	500 m–3 km	*Pilkington and Todoeschuck* [1995]
4[c]	Metamorphic, intrusive, volcanic	Flin-Flon Snow Belt, Canada	500 m–3 km	*Pilkington and Todoeschuck* [1995]
		Aeromagnetic Data		
1.5[d]	Sedimentary (sandstone)	Bohemian Massif, Germany	6.4 km	*Maus and Dimri* [1995]
2.8[d]	Metamorphic (gneiss, metabasite)	Bohemian Massif, Germany	6.4 km	*Maus and Dimri* [1995]
3[d]	Igneous (granite, few metabasite)	Bohemian Massif, Germany	6.4 km	*Maus and Dimri* [1995]
3.2[d]	Metamorphic covered by sediments	Sakatchewan, Canadian shield	50 km	*Maus and Dimri* [1996]
3.8[e]	Metamorphic and Intrusive	Ontario, Canadian shield	8 km	*Gregotski et al.* [1991]
3.9[e]	Metamorphic covered by sediments	Sakatchewan, Canadian shield	50 km	*Gregotski et al.* [1991]
4[e]	Metamorphic covered by sediments	Sakatchewan, Canadian shield	50 km	*Pilkington et al.* [1994]
4[f]	Variable	Canadian shield	500 km	*Pilkington and Todoeschuck* [1993]
4.1[e]	Metamorphic	Ontario, Canadian shield	8 km	*Gregotski et al.* [1991]
4	Variable	Central Asia	∼4000 km	*Maus et al.* [1997]
4	Principally Igneous	South Africa (with LIP Karoo)	∼1000 km	*Maus et al.* [1997]
5.5–5.8[d]	Igneous	Hawaii	17 km	*Maus and Dimri* [1996]

[a]In order to ease the comparison of estimates obtained by various studies using different terminologies, we converted their estimate into an estimate of the parameter β, defined as the slope of the 3-D power spectrum of the magnetization in equation (1), as specified in the footnotes. Scale values correspond to the range of wavelengths used to estimate the fractal parameter from susceptibility data and to the size of the computational window used to perform the spectral analysis of aeromagnetic anomalies. The fractal parameter β was derived from the parameters used in other studies in the following way:

[b]From the slope of the 1-D power spectrum of the magnetization $\beta 1D$, deduced from borehole data by $\beta = \beta 1D + 2$ (as demonstrated by *Maus and Dimri* [1994]).

[c]From the slope of the 2-D power spectrum of the magnetization $\beta 2D$, deduced from map of susceptibility data by $\beta = \beta 2D + 1$ (as demonstrated by *Maus and Dimri* [1994]).

[d]From the parameter γ by: $\beta = \gamma + 1$.

[e]From the parameter α by $\beta = -\alpha + 1$.

[f]From the parameter α by $\beta = -\alpha$.

of borehole magnetic susceptibility profiles, maps of magnetic susceptibility measurements, and aeromagnetic data. Table 1 presents a summary of published estimates for the fractal parameter β, as defined in equation (1). Note that indirect estimates of this parameter deduced from the analysis of aeromagnetic anomalies may be biased by assumptions made by the authors on the depth to the top and to the bottom of magnetic sources. Fractal parameters deduced from susceptibility measurements performed on a wide range of lithologies vary from ∼2.5 to ∼5.0 but do not seem to be simply related to rock type. Variations of the fractal parameter between these different studies may therefore be attributed to other causes, such as fractures, deformation, alteration, or also range of wavelengths accessible in the studies (in the case where crustal magnetization is multifractal as proposed by *Gettings* [2005] and *Pecknold et al.* [2001]). Fractal parameters derived from aeromagnetic studies (in Table 1) also show a large range of values. However, estimates obtained within large computational windows (with dimensions from 50 km to ∼4000 km), which may be representative of deep crustal magnetic sources, are often close to 4, suggesting that a constant value of 4 is representative of the fractal parameter for the deep crust. Note however that these later studies were performed in only three regions (Canadian shield, Central Asia, and South Africa) characterized by a deep crust probably very different from our study area. Nevertheless,

these various studies show that the fractal parameter β may potentially vary across the study area.

4. Results in the Great Basin

[24] In this section, we discuss results obtained by applying this methodology to the Great Basin and surrounding areas (study area indicated by the red rectangle in Figure 1). Results are presented as maps of the depth to the top z_t and to the bottom z_b of magnetic sources, and of the misfit between calculated and theoretical power spectra. The depths z_t and z_b are relative to topography. Maps are presented with pixilated pictures, showing values obtained in individual windows (spaced 25 km apart), in order to show whether these maps display smooth variations as expected using overlapping windows. Results obtained from windows including deep oceanic areas are likely biased, as magnetization acquired during seafloor spreading is not fully random in all directions, as assumed by the methodology, but instead displays a degree of two dimensionality. We will therefore only discuss results obtained over the continental part of our study area.

[25] As we have shown previously with synthetic data sets, it is not possible to solve accurately for all three unknown parameters. We therefore assumed that the fractal parameter β is constant across the entire study area and solved for the two other parameters. The value of the fractal
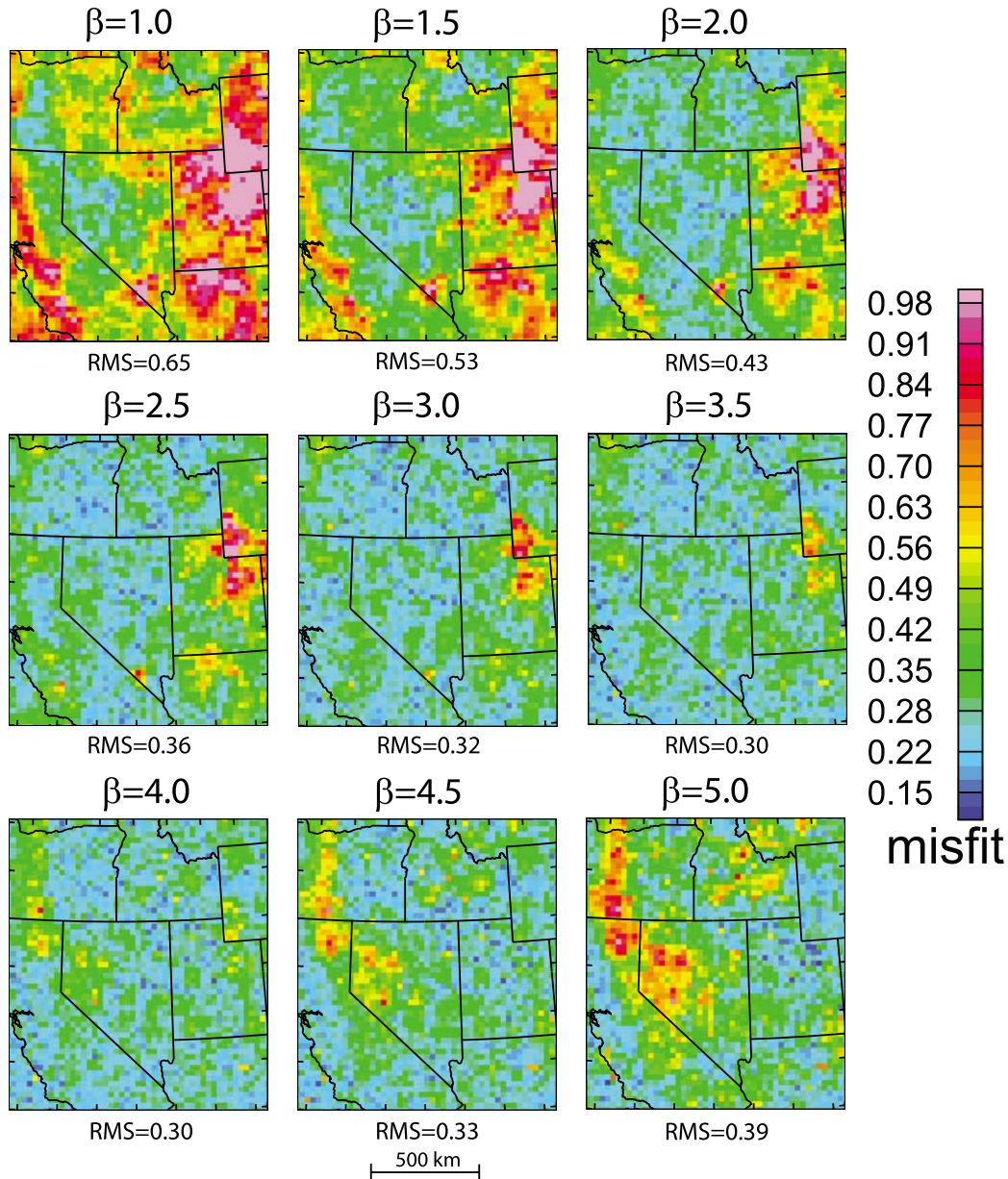
Figure 8. Maps of the misfit between the theoretical curves and the radial power spectra obtained using moving windows of 100 km over the North America compilation and assuming various constant values for the fractal parameter β within the study area located in Figure 1. For each map, the root-mean-square (RMS) of misfit values is also specified. Low misfits across the entire study area are obtained for a constant fractal parameter β between 3.0 and 4.0.

parameter was chosen so that the misfit between the best fit theoretical curve and the calculated radial power spectrum is low over the entire study area. Figure 8 shows maps and root-mean-squares (RMS) of the misfits obtained over the study area for different values of the fractal parameter β using a window size of 100 km. These maps show that low misfits across the entire study area are obtained for a constant fractal parameter β between 3.0 and 4.0. These values are consistent with values obtained by previous studies in other areas (see Table 1), and in particular, with a constant fractal parameter representative of deep crustal magnetic sources of ~4, as suggested by previous studies of aeromagnetic anomalies within large computational win-

dows. Although a slightly lower RMS of misfits is obtained for a fractal parameter of 3.5 or 4.0 (Figure 8), we chose to present the results with $\beta = 3.0$, because this value provides depths to the bottom of magnetic sources z_b that are closer to values of the depth to the Curie temperature isotherm derived from heat flow data [e.g., *Blackwell and Richards*, 2004]. For other values of β (<3.0 or > 4.0), maps of misfits display long-wavelength features that are inversely related for low (<3.0) and large (>4.0) values of β, suggesting that the appropriate fractal parameter may potentially vary within the study area, as we will discuss later. Note that a value of $\beta = 1.0$ leads to high misfits over most of the study area, except in the Cascade Range and western Nevada
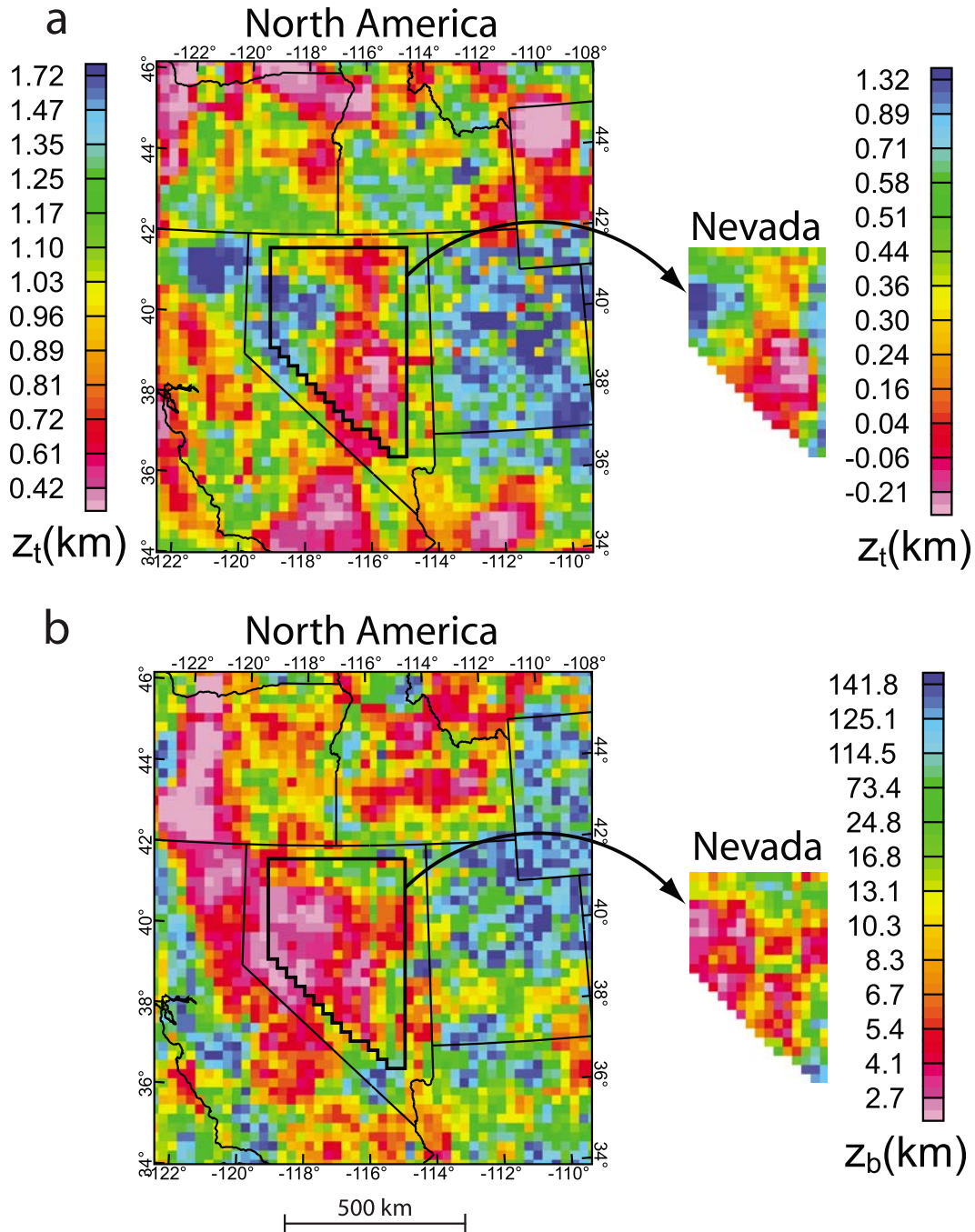
Figure 9. Maps of the (a) depth to the top z_t and (b) depth to the bottom z_b of magnetic sources obtained from the North America (on the left) and Nevada (polygon on the right) compilations using moving windows of 100 km and assuming $\beta = 3.0$. Values of z_t and z_b are relative to topography. Note that maps of z_b obtained from Nevada and North America compilations (Figure 3b) are represented by the same color scale. Maps obtained from both compilations display similar long-wavelength features.

where *Connard et al.* [1983] and *Blakely* [1988] obtained estimates of the depth to the Curie temperature isotherm within the range of depths expected from heat flow. This indicates that the shape of the power spectrum for an uncorrelated magnetization, as assumed in early studies, does not reproduce well the shape of radial power spectra obtained from aeromagnetic data in most of the study area, except in the Cascade Range and western Nevada.

[26] Figure 9 shows maps of the depth to the top z_t and to the bottom z_b of magnetic sources obtained with a moving window of 100 km and assuming a constant fractal parameter $\beta = 3.0$. These two maps display long-wavelength features with dimensions of the order of several hundreds of kilometers (larger than the size of the window or the size of the surveys) indicating that these features probably correspond to real geophysical signals. Although not directly
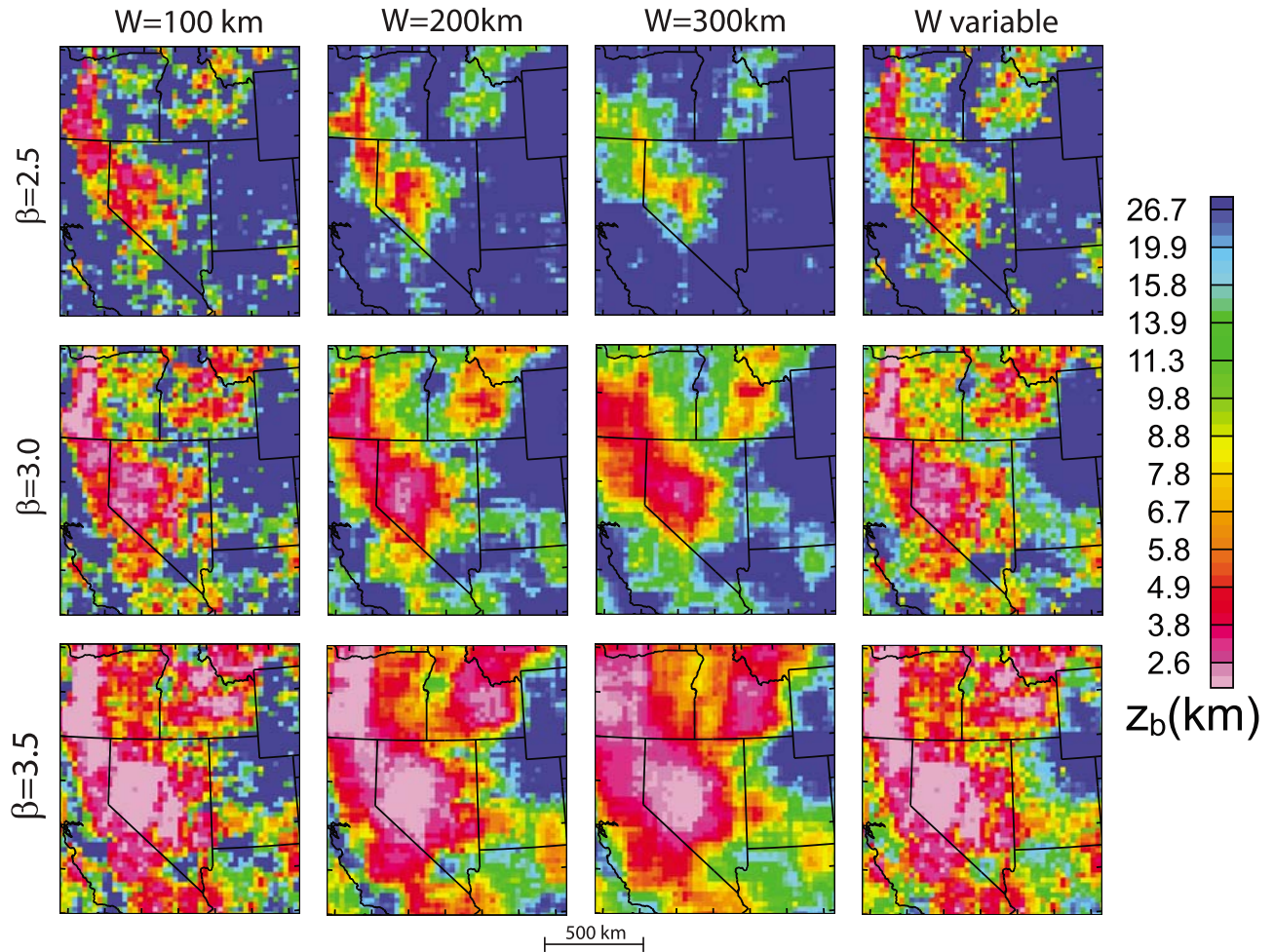
Figure 10. Maps of the depth to the bottom of magnetic sources z_b obtained assuming various constant values for the fractal parameter ($\beta = 2.5, 3.0, 3.5$) and using various size of moving windows ($W = 100$, 200, 300 km) over the North America compilation and within the study area located on Figure 1. Values of z_b are relative to topography. Maps from the right column were obtained with a variable window size that was chosen in the following way. For each grid point in the final map, we increased progressively the size of the window (starting from a window size of 100 km and increasing its size by 50 km increments) until we obtain a depth z_b that is smaller than a tenth of the size of the window with a maximum window size of 300 km. All maps display similar long-wavelength features that are independent of the values of W and β. These maps were obtained with the same color scale ranging from 0 km to 30 km as the maximum window size of 300 km does not allow resolving depths deeper than 30 km.
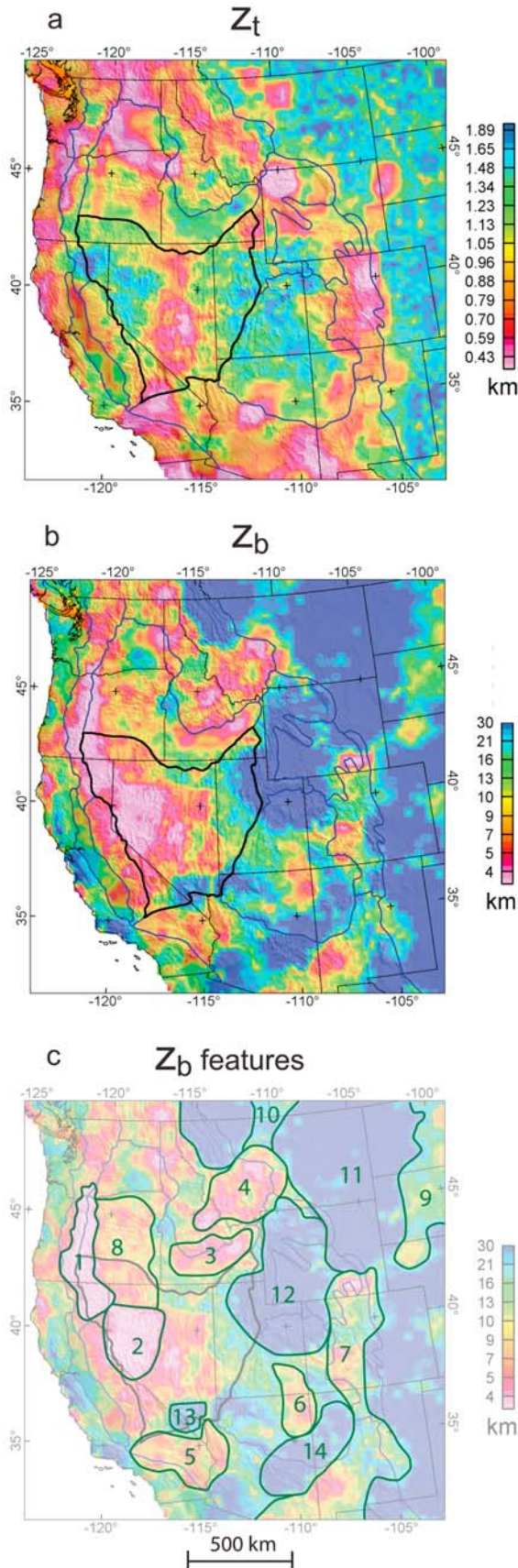
correlated, these two maps show a number of correlated features (shallow z_t associated with deep z_b), indicating that uncertainties due to nonuniqueness of the problem might affect our results. In areas where z_b is deeper than about 10 km, the map of z_b shows significant noise and unrealistically large depths (up to ~ 150 km). Based on our test on synthetic data sets, the method requires a window size about 10 times larger than the depth extent of magnetic sources to provide accurate estimates. In these areas, the window size (100 km) is probably too small to distinguish the shape of the power spectrum from those obtained for a half-space and therefore to constrain the depth extent of magnetic sources. Note that since these maps were obtained assuming a constant fractal parameter, some of the spatial variations in z_t or z_b may be due to spatial variations in β.

[27] Maps of the depth to the top z_t and to the bottom z_b of magnetic sources obtained using the Nevada or the North

America aeromagnetic compilations display similar long-wavelength structures (Figure 9). Absolute values of z_b are similar for both compilations, whereas absolute values of z_t appear to be shallower for the Nevada compilation than for the North America compilation. This artifact might be due to the divergence observed at short wavelengths between the Nevada and North America compilations (Figure 3b), although we limited the range of frequency used to perform the fit in order to avoid such discrepancies. Nonetheless, this problem does not seem to affect results for z_b which shows that we can confidently use the North America compilation (instead of state compilations) to study spatial variations of the depth to the bottom of magnetic sources.

[28] Last, we investigated the influence of the size of the window W and of the fractal parameter β (assumed constant across the entire study area) on the map of the depth to the bottom z_b (Figure 10). These maps display similar long-

wavelength patterns, for all values of W or β, indicating that these patterns are robust and have geophysical significance. As expected, the observed patterns become smoother as W increases. On the other hand, the absolute value of z_b generally decreases as β increases, reflecting the fact that assuming a larger β than the correct value is compensated by negative errors in z_b. Finally, in order to obtain the best resolved map of the depth to the bottom of magnetic sources, we computed a map of z_b (right column on Figure 10) using a variable size of the moving window in the following way. For each grid point in the final map, we progressively increased W until we obtained a depth z_b that is smaller than a tenth of the window size ($W \geq 10\, z_b$) to ensure well-resolved depths z_b with uncertainties of the same order of magnitude for different ranges of depths. As a consequence, areas characterized by shallow z_b are mapped with a better spatial resolution than areas characterized by deep z_b. In practice, we started with $W = 100$ km and we increased W by 50 km increments up to a maximum of 300 km. Therefore, only depths shallower than 30 km are well resolved in these maps.

5. Discussion

[29] Based on the previous analysis, our preferred result assumes $\beta = 3.0$ and uses variable window size (the map in the last column and second row of Figure 10). In this section, we compare our final map of the depths to the top z_t (obtained using a window size of 100 km) and to the bottom z_b (obtained using a variable size of window ranging from 100 km to 300 km) to various geologic and geophysical data in order to better understand the origin of their long-wavelength features and, in particular, to determine which of these features are due to spatial variations of the depth to the Curie temperature isotherm. We present here results obtained for the entire western United States (Figure 11). Prominent features in z_b described in the text are labeled in Figure 11c and Table 2.

5.1. Comparison of Results With Aeromagnetic Data

[30] We first compare our results with the original aero-magnetic compilation used to perform the computations (Figure 12a). Areas mapped as shallow z_b (in red-pink) generally correspond to areas dominated by short-wavelength anomalies, such as in the Cascade Range (feature 1, Figure 11), in the western Great Basin (feature 2, Figure 11, including the Walker Lane Belt; also see Figure 12f), and in the Snake River Plain (feature 3, Figure 11). On the other hand, areas mapped as deep z_b generally correspond to areas dominated

Figure 11. Maps of the depth to the (a) top z_t and to the (b) bottom z_b of magnetic sources for the whole western United States. Values of z_t and z_b are relative to topography. These maps were obtained assuming a constant value of the fractal parameter $\beta = 3.0$ and using a window size of 100 km (map a for z_t) and a variable size of window ranging from 100 km to 300km (map b for z_b). Blue outlines delineate the physiographic provinces modified from *Fenneman and Johnson* [1946]. The black thick outline delineates the Great Basin. (c) Prominent features (green outlines) of the map of the depth to the bottom of magnetic sources referred in the text and in Table 2.

Table 2. Descriptions of Prominent Features Observed in the Map of z_b Localized on Figure 11c: Location, Magmatic and Tectonic Activities, and Possible Origin of the Features

| Number	Physiographic Province	Heat Flow Data	Magmatic Activity	Tectonic Activity	Interpretation
			Very Shallow z_b		
1	Cascade Ranges	Very high	Cascade Arc (active)		Shallow Curie temperature isotherm
2	Western Great Basin	High to low (nearby the Eureka Low)	Ancestral Cascade Arc (~21 Ma), Northern Nevada Rift (~17 Ma), Basin and Range volcanism (~17–0 Ma)	Basin and Range extension (~17–0 Ma), Walker Lane Belt, Seismic belt in Central Nevada	Shallow Curie temperature isotherm
3	East Snake River Plain	Very high	Track Yellowstone hot spot (12–0 Ma)	No current seismicity	Shallow Curie temperature isotherm
4	South part of Northern Rocky Mountains	Intermediate	Tertiary Plutons (40–50 Ma)	Basin and Range extension	Influence of lithology or tectonic fabric
			Relatively Shallow z_b		
5	North part of Sonoran Deserts	Intermediate	Tertiary and quaternary volcanism	Basin and Range extension	Shallow Curie temperature isotherm
6	Center of Colorado Plateau	Low	Navajo (~20–30 Ma) and Hopi Buttes (~2–5 Ma) volcanic fields	Stable since Precambrian	Relatively shallow Curie temperature isotherm
7	Rio Grande Trough	High	Magmatism (30–20 and 10–3 Ma)	Extension (30–20 Ma and 10–3 Ma)	Shallow Curie temperature isotherm
8	Columbia River Plateau	High to intermediate	Columbia River and Steens Mountain basalts (~17 Ma)		Shallow Curie temperature isotherm
			Relatively Deep z_b		
9	Great Plains	Mostly low, locally high	A few Tertiary plutons and volcanics (~50 Ma)	Stable since Precambrian	Influence of lithology or tectonic fabric
10	Great Plains	Low	A few Tertiary plutons	Stable since Precambrian	Influence of lithology or tectonic fabric
			Very Shallow z_b		
11	Great Plains	Low to intermediate	No volcanics or plutons outcroping	Stable since Precambrian	Deep Curie temperature isotherm
12	Wyoming Basin, Middle Rocky Mountains, Northern Colorado Plateau, Eastern Great Basin	Mostly low	No volcanics except on the edges of the zb feature	Sedimentary basin	Deep Curie temperature isotherm
13	Southernmost Nevada	Intermediate	No volcanics or plutons outcroping	Basin and Range extension	Influence of lithology or tectonic fabric
14	Southern Colorado Plateau	Intermediate	Quaternary volcanic rocks		Influence of lithology or tectonic fabric
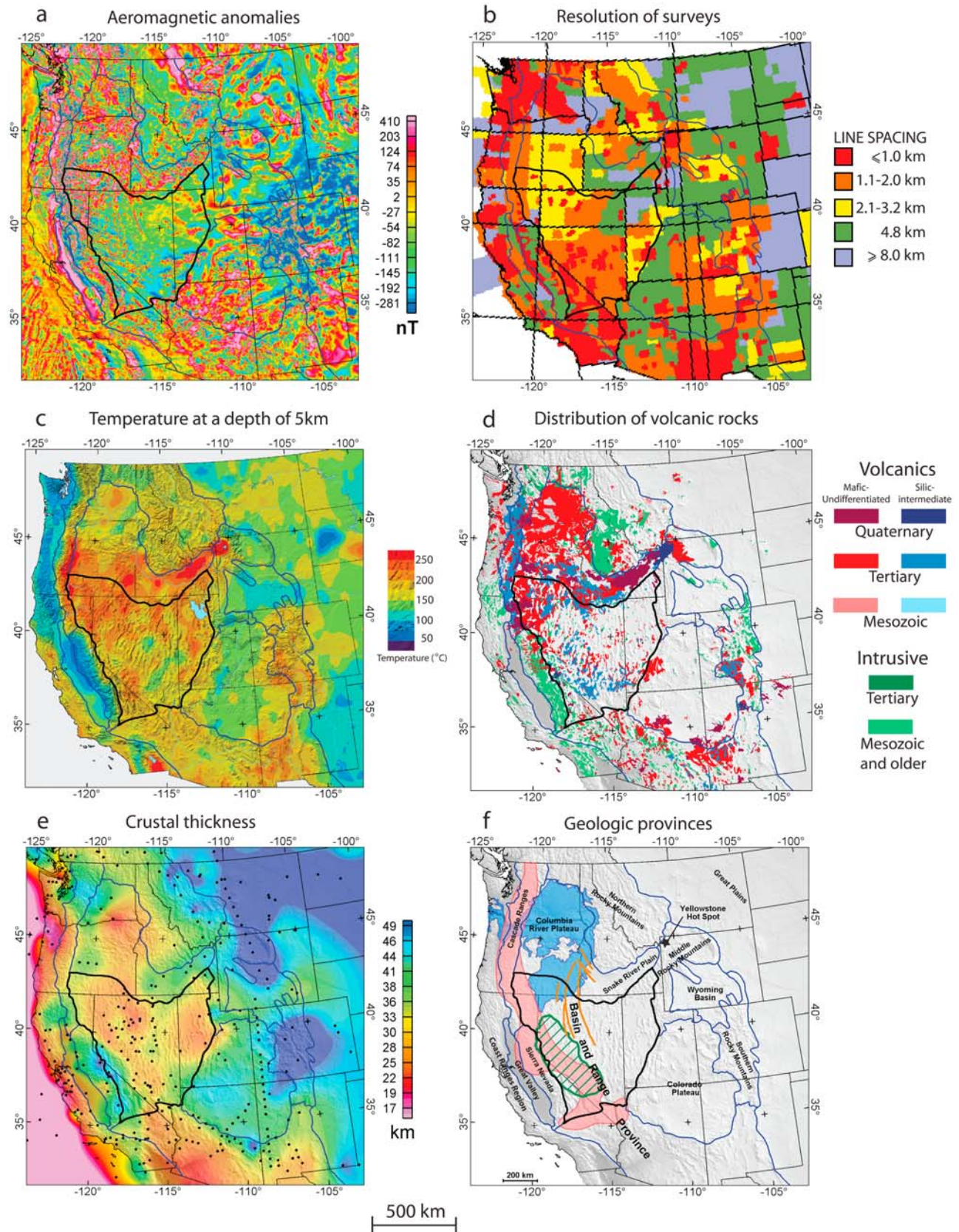
Figure 12

by long-wavelength anomalies, such as in the Great Plains (feature 11, Figure 11), in the Wyoming Basin (feature 12, Figure 11), and in southernmost Nevada (feature 13, Figure 11). These visual correlations are expected since our methodology is based on the analysis of the spectral content of aeromagnetic anomalies. One may however wonder if the spatial variations in z_t and z_b are due to true variations in the spectral content of magnetic anomalies or are artifacts due to variations in the survey resolution. Although, we do not observe a direct correlation between flight line spacing (Figure 12b) and z_t (Figures 11a), several features of the map of z_t seem to be due to variations in the survey resolution. Areas mapped as very shallow z_t generally correspond to areas with high-resolution magnetic surveys (line spacing smaller than 1.0 km), such as in Yellowstone National Park in northwestern Wyoming. Likewise, areas mapped as deeper z_t correspond with areas with only medium- to low-resolution magnetic surveys, such as the volcanic plain of the Snake River where very shallow magnetic sources are nevertheless expected. This simply reflects that shallow magnetic sources are well resolved only by very high resolution surveys. The aeromagnetic compilation for North America is therefore inadequate to recover the long-wavelength variations in the depth to the top of magnetic sources. On the other hand, prominent features in z_b do not seem to be due to variations in survey resolution, as different areas covered with similar survey resolutions are mapped with various values of z_b (from very shallow to very deep).

5.2. Comparison of Results With Heat Flow Data

[31] The original purpose of this study was to provide an independent assessment of crustal temperatures, under the assumption that the bottom of magnetic sources z_b corresponds to the Curie temperature isotherm. Figure 12c shows temperatures at 5 km depth, estimated from heat flow [*Blackwell et al.*, 2007], and Table 3 shows approximate values of the depth to the Curie temperature isotherm inferred from heat flow data in selected areas. In Table 3, approximate values for the depth to the Curie temperature isotherm were obtained from the surface heat flow Q_0 using the expression [e.g., *Lachenbruch and Sass*, 1977]

$$T(z) = \frac{Q_0 - DA_0}{K}z + \frac{D^2A_0\left(1 - e^{-Z/D}\right)}{K} \qquad (10)$$

which describes crustal temperature T versus depth z assuming heat transport by conduction and exponential decay of radioactive heat production with depth. We also assumed, following *Lachenbruch and Sass* [1977], a constant thermal conductivity $K = 2.5$ W.m^{-1}.K^{-1}, a constant surface heat production $A_0 = 2$ μW.m^{-3}, a constant characteristic depth for heat production $D = 10$ km, and a Curie temperature of 580°C (Curie temperature of magnetite). Note that these parameters are likely to vary with geologic setting and depth. This calculation provides therefore only a first-order estimate of the depth to the Curie temperature isotherm. A relative comparison of the maps of the depth to the bottom of magnetic sources z_b and of the temperature at 5 km (Figure 12c) reveals several striking correlations in long-wavelength patterns. Shallower z_b are generally observed in areas characterized by elevated crustal temperature, such as in the Cascade Range (feature 1, Figure 11), along the Snake River Plain (feature 3, Figure 11), and along the Rio Grande Trough (feature 7, Figure 11). Deeper z_b are generally observed in areas characterized by lower temperature, such as in the Great Plains (feature 11, Figure 11) and the Wyoming Basin (feature 12, Figure 11). Several discrepancies also are observed between the two maps. Several long-wavelength features observed in the map of the depth to the bottom of magnetic sources z_b (see for instance features 2, 4, 6, 9, 10, 13 and 14, Figure 11) are not observed in the crustal temperature map derived from heat flow data (Figure 12c). Some prominent heat flow features are absent from the map of the depth to the bottom of magnetic sources, such as the very high heat flow over the Yellowstone hot spot (northwest corner of Wyoming, see location on Figure 12f) and over the Salton Trough (southernmost California), and the low heat flow over the Sierra Nevada and Great Valley. In addition, absolute values of the depth to the bottom of magnetic sources z_b obtained for $\beta = 3.0$ in areas with shallower z_b are generally much smaller than depths to the Curie temperature isotherm estimated from heat flow data (Table 3).

5.3. Possible Origins of Discrepancies

[32] Discrepancies between depths to the Curie temperature isotherm estimated from heat flow and aeromagnetic data are not surprising since heat flow and crustal temperatures are still relatively poorly constrained in several areas in the western United States. Scarcity of heat flow data in the Colorado Plateau and the Great Plains may explain why some features in z_b (such as features 6, 9, 10, and 14, Figure 11)

Figure 12. Maps showing geophysical and geologic data within the western United States. Blue outlines delineate the physiographic provinces modified from *Fenneman and Johnson* [1946]. The black thick outline delineates the Great Basin. (a) Map of magnetic anomalies at the elevation of 305 m above the ground obtained from the compilation of aeromagnetic surveys in North America [*NAMAG*, 2002]. (b) Map of flight line spacing within the North America aeromagnetic compilation. (c) Map of the temperature estimated at 5 km created by the Idaho National Laboratory (http://geothermal.inel.gov/maps/) from the regional heat flow database from the SMU Geothermal Laboratory (http://smu.edu/geothermal/) accessed on the 12 April 2005 (see *Blackwell et al.* [2007] for calculation method). (d) Map showing the distribution of volcanic and intrusive rocks separated as a function of their chemistry and age (modified from *Schruben et al.* [1998]). (e) Map of the crustal thickness based on data (black dots) from the seismic database compiled by *Chulick and Mooney* [2002]. (f) Shaded relief map showing physiographic provinces, the Northern Nevada Rift (as mapped by *Glen and Ponce* [2002]; orange curves), the present location of the Yellowstone hot spot (black solid star), the Columbia River and Steens Mountain basalts [*Camp and Ross*, 2004] (in blue), the presumed location of the ancient Cascade Arc (as proposed by *Christiansen and Yeats* [1992]; in pink) and the magnetic pattern related to the Walker Lane Belt [from *Glen et al.*, 2004] (green hachured zone).

Table 3. Table of Heat Flow, Depths to the Curie Temperature Isotherm, Moho and Expected Basal Depth of Magnetic Sources in Selected Physiographic Provinces[a]

Area	Heat Flow (mW/m^2)	Curie Depth (km)	Moho Depth (km)	Basal Depth (km)
Great Basin				
Typical	$75-95$[b]	$17-23$	$25-35$[j,k]	$17-23$
Battle Mtn High	$105-160$[c,d]	$10-15$	$19-23$[j,k]	$10-15$
Eureka Low	$30-65$[c,d]	$28-125$	$25-35$[j,k]	$25-35$
Eastern Snake River Plain	$\sim75-110$[e]	$15-23$	~42[l,m]	$15-23$
Cascade Range				
High Cascades	~100[f,g]	~16	~45[n,o]	~16
Western Cascades	$40-50$[f,g]	$41-63$	~45[n,o]	$41-45$
Great Valley	$25-55$[h]	$36-250$	~35[p,q]	~35
Colorado Plateau	~60[i]	~32	$40-50$[r,s]	~32

[a]Provinces are located in Figure 1. Heat flow data and depth to Moho are extracted from the literature cited below the table. Approximate values expected for the depth to the Curie temperature isotherm are extrapolated from heat flow data (upper bound for Curie depth estimated from lower bound of heat flow and vice versa) using equation (10) which assumes heat transport by conduction and exponential decay of radioactive heat production with depth, with a constant thermal conductivity of $K = 2.5$ W.m^{-1}.K^{-1}, a constant surface heat production of $A_0 = 2$ μW.m^{-3}, a constant characteristic depth for heat production of $D = 10$ km, and a Curie temperature of 580°C (Curie temperature of the magnetite). Note that these depth estimates are overestimated for the cases where the Curie temperature isotherm is below the Moho because expression (10) with the specified thermal parameters is only valid for crustal temperatures. Approximate values expected for the basal depth of magnetic sources are inferred from the smallest value obtained for the depths to the Curie temperature isotherm and to the Moho.

[b]*Blackwell* [1983].
[c]*Sass et al.* [1971].
[d]*Lachenbruch and Sass* [1978].
[e]*Blackwell* [1989].
[f]*Blackwell et al.* [1982].
[g]*Blackwell et al.* [1990].
[h]U.S. Geological Survey Heat Flow Database for California (2003) (available at http://quake.wr.usgs.gov/heatflow).
[i]*Bodell and Chapman* [1982].
[j]*Heimgartner et al.* [2006].
[k]*Benz et al.* [1990].
[l]*Braile et al.* [1982].
[m]*Peng and Humphreys* [1998].
[n]*Leaver et al.* [1984].
[o]*Schultz and Crosson* [1996].
[p]*Godfrey et al.* [1997].
[q]*Fliedner et al.* [2000].
[r]*Wolf and Cipar* [1993].
[s]*Parsons et al.* [1996].

are absent from the crustal temperature map (Figure 12c). Poor constrains on thermal conductivities and heat production also render large uncertainties on crustal temperature estimates derived from heat flow data [e.g., *Blackwell et al.*, 2007]. Some areas may display spatial variations in shallow crustal temperatures that do not reflect variations in the depth to the Curie temperature isotherm because of complex 3-D variations in thermal conductivity, rapid erosion or sedimentation, variations in the radioactive heat production, heat provided by recent volcanism (such as in the Great Basin, Snake River Plain, Cascade Ranges, and Rio Grande Rift), or groundwater circulation. For instance, the Eureka Low heat flow area (Figure 1) [*Sass et al.*, 1971] is not associated with deeper z_b but instead very shallow z_b (see feature 2 in the western Great Basin), suggesting that this feature does not reflect regional variations in the lower crustal heat flow but instead upper crustal temperature perturbations due to groundwater circulations as proposed by *Sass et al.* [1971] and *Lachenbruch and Sass* [1977]. However, approximate values for heat flow in large provinces (see Table 3) and several prominent features that are well constrained in the crustal temperature map derived from heat flow data (Figure 12c) are not well reproduced in the map of z_b. Such discrepancies may have a different origin, such as the limited spatial resolution inherent in our method or the simplicity of the crustal magnetization model assumed in this study.

[33] Since the minimum window size used in this study is 100 km, our method provides only a smoothed image of variations in z_b and in particular does not permit distinguishing features smaller than the window size. This may explain why our map of z_b is missing some robust but relatively narrow heat flow features, such as the Yellowstone hot spot or the Salton Trough. Moreover, since large windows are needed to resolve deep magnetic sources, it is difficult to obtain accurate estimates of the depth to the bottom of magnetic sources z_b for narrow structures with deep bottoms of magnetic sources, such as the Great Valley. In this case, a small window size, such as 100 km, is insufficient to resolve the bottom of magnetic sources but a larger window includes areas outside the edge of the valley and provides therefore an averaged depth z_b not representative of the valley.

[34] In some regions, the bottom of magnetic sources may be a lithologic contact. For instance, our method will not ascertain the depth to the Curie temperature isotherm if the isotherm lies in the mantle, because unaltered mantle rocks in continental region are generally considered nonmagnetic [e.g., *Wasilewski and Mayhew*, 1992]. In this case, the bottom of magnetic sources will more likely correspond to the base of the crust (Figure 12e and Table 3). This should not be a problem in areas of high heat flow, where the Curie temperature isotherm is expected to be shallower than mantle depths (e.g., most of the Great Basin, Snake River
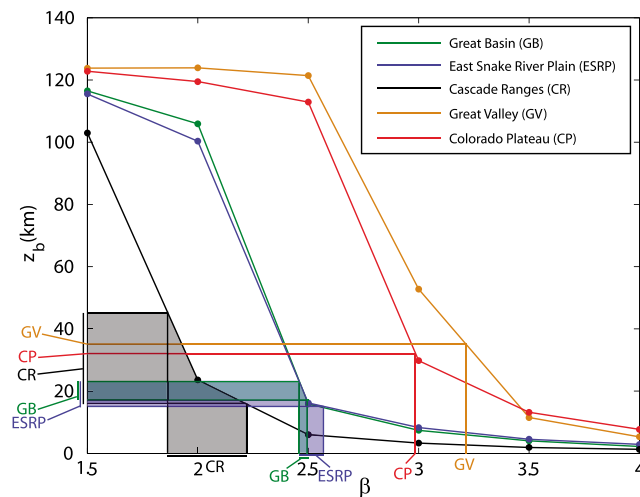
Figure 13. Curves representing the evolution of the median of the depths to the bottom of magnetic sources, z_b, obtained in a few physiographic provinces (GB, Great Basin; ESRP, East Snake River Plain; CR, Cascades Ranges; GV, Great Valley; CP, Colorado Plateau) as a function of the assumed value of the fractal parameter β. Values of z_b are relative to topography. Curves were computed using maps of z_b obtained within the study area located in Figure 1 and using a window size of 100 km. These curves are used to determine, in different provinces, values of β (indicated by the colored bars along the β axis) that provide values of z_b within the range of basal depths derived from heat flow and Moho depth (indicated by the colored bars along the z_b axis; Table 3). See location of the physiographic provinces in Figure 1.

Plain and Cascade Range; see Table 3). It might be an issue in areas characterized by low heat flow, where the Curie temperature is expected to be deeper than mantle depths (e.g., in the Great Valley; see Table 3). Moreover, our methodology assumes a model of crustal magnetization composed of a single layer of fractal random magnetization. The Earth's magnetic crust is of course much more complex. For instance, strongly magnetic igneous rocks may intrude and overlie a less magnetic metamorphic basement and very weakly magnetic basin sediments. The Fourier transform of the magnetic anomalies over such complex crust is the sum of the contribution of all these units. However, in some cases, the magnetic signal due to one of the units may be so strong as to mask the magnetic signal due to other units. This might be the case for areas covered by young volcanic rocks. In this case, our methodology might give a z_b that corresponds to the base of the dominant unit, i.e., the volcanic rocks. The very shallow z_b (on the order of a few km) observed over some volcanic areas (see features 1, 2, 3, 7, Figure 11) could therefore be explained by the dominance of the magnetic signal associated with volcanic rocks. Our method would then provide an estimate of the thickness of superficial volcanic rocks instead of the depth to the Curie temperature isotherm. Note however that the Columbia River basalts are associated with deeper z_b (see feature 8, Figure 11) than other volcanic provinces such as the Cascade Ranges (feature 1, Figure 11), the western

Great Basin (feature 2, Figure 11), and the Snake River Plain (feature 3, Figure 11).

[35] Although several studies of susceptibility and aeromagnetic data sets suggest that crustal magnetization may be characterized by a constant fractal parameter β close to 4 (see Table 1), it is possible that different geologic terranes are characterized by different fractal parameters. Therefore, since the map of z_b has been obtained assuming β constant over the entire western United States, there is some ambiguity when interpreting its long-wavelength features. Spatial variations in z_b may be attributed to either actual variations in the depth extent of magnetic sources or to variations of the geology affecting β. In particular, shallow z_b are generally observed over regions covered by volcanic rocks, which typically have short-wavelength variations in magnetic properties and may therefore be characterized by low values of β (see features 1, 2, 3, 5, 7, and 8, Figure 11, and Figure 12d). Deep z_b are generally observed over regions lacking volcanic rocks (see features 11, 12, and 13, Figure 11). Note, however, that a correlation of z_b with the distribution of volcanic rocks is not in contradiction with a correlation with the heat flow since young volcanic areas are usually characterized by high heat flow (associated to tectonic extension or residual heat from magmatic intrusions). Also, several features with shallow z_b are not associated with a significant amount of volcanic rocks (see features 6 and 9, Figure 11). In the case where the fractal parameter can be assumed constant over the entire western United States or simply over large geologic provinces, our poor knowledge of the appropriate value for β is still a source of uncertainty on the absolute value of z_b. Indeed, we see in Figure 10 that z_b is significantly increased if we assign a smaller value to β. An inappropriate value for β may therefore explain why our map of the depth to the bottom of magnetic sources shows areas with z_b much smaller than depths to the Curie temperature isotherm inferred from heat flow data (see Table 3). Figure 13 shows the median of the depths z_b obtained in different physiographic provinces assuming different values of the fractal parameter β and using a constant window size of 100 km. We searched the values of β that provide averaged values of z_b in various provinces that are in the range of depths deduced from heat flow and mantle depth in Table 3. Such values of z_b were obtained with $\beta \approx 2.0$ in the Cascade Ranges, $\beta \approx 2.5$ in the Great Basin and the East Snake River Plain, $\beta \approx 3.0$ in the Colorado Plateau, and $\beta \approx 3.25$ in the Great Valley. Note that these values are all inferior to 3.5 justifying our constant value of 3.0, rather than 3.5 or 4.0, to be better representative of the western United States crustal magnetization, assuming that the bottom of magnetic sources corresponds to the Curie temperature isotherm. Also, this suggests that lower values of β are more appropriate over volcanic regions, whereas larger values of β are more appropriate over tectonically stable regions. This is also supported by Figure 8 showing relatively low misfits over regions covered by volcanic rocks such as in the Cascade Ranges, Nevada and the Snake River Plain for low values of β (<2.0).

[36] The very shallow depths to the bottom of magnetic sources in high heat flow areas (see in particular features 1, 2 and 3, Figure 11) also could indicate that the characteristic Curie temperature for our study area is lower than the Curie

temperature of magnetite, $\sim580°C$, usually assumed to be representative of crustal magnetization. Studies of xenoliths, high-grade metamorphic terrains, and obducted lower crust suggest that the principal source of magnetization in the middle and lower crust is low-titanium titanomagnetite, with Curie temperatures of $\sim400–580°C$ (corresponding to $\sim420–600°C$ at 35 km depth) [e.g., *Frost and Shive*, 1986; *Shive et al.*, 1992; *Wasilewski and Mayhew*, 1992]. Furthermore, it is possible that the titanium content of magnetic minerals decreased in these exposed lower crustal rocks as they rose to the surface and cooled [e.g., *Shive et al.*, 1992]. The Curie temperature at depth could therefore be even lower if high-titanium titanomagnetite is abundant [e.g., *Dunlop and Özdemir*, 1997]. Other magnetic minerals with significantly lower Curie temperature may also be important components of the crustal magnetization. Titanium-rich hemoilmenites have strong magnetization but low Curie temperature <220°C [e.g., *Hunt et al.*, 1995] and may therefore significantly contribute to upper crustal magnetization. On the other hand, recent studies have proposed that exsolutions of hematite and ilmenite, with Curie temperature of $\sim580–680°C$ may significantly contribute to lower crustal magnetization [e.g., *Kletetschka et al.*, 2002; *McEnroe et al.*, 2004]. The bottom of magnetic sources could also correspond to a transition in the magnetic mineralogy. For instance, transformation of maghemite into weakly magnetic hematite occurs at temperature between $\sim250–750°C$ [e.g., *Dunlop and Özdemir*, 1997]. The lower crust might also display lateral variations in magnetic mineralogy or titanium content, causing different temperatures for the base of magnetic sources in different geological settings. For instance, Curie temperatures reported by *Wasilewski and Mayhew* [1992] in lower crustal xenoliths are $\sim575°C$ for the Colorado Plateau, $450–550°C$ for California, and $<200°C–570°C$ for the Rio Grande Rift. The very shallow basal depth of magnetic sources obtained in several areas could therefore possibly be explained by a lower Curie temperature in these areas.

[37] Finally, our depth estimations may be biased by other complexities in the crustal magnetization not taken into account by our method. The crust is composed of multiple layers that may be characterized by different magnetic properties (different fractal parameters) yielding a radial power spectrum possibly more complicated than predicted by equation (4). The fractal parameter might vary with the wavelength [e.g., *Gettings*, 2005; *Pecknold et al.*, 2001] or depend on the direction (i.e., vertical versus horizontal) [e.g., *Lovejoy et al.*, 2001]. The model parameters z_t, Δz, and β might vary within the computational window. The crustal magnetization might display very large features whose widths are on the order of or larger than the size of the window, indicating that magnetization cannot be considered random at the scale of the window size. Our method also assumes that the magnetization is parallel or antiparallel to the magnetic field. This method is therefore valid only in areas where induced magnetization dominates over remanent magnetization, where remanent magnetization is carried by young rocks that have not been affected by deformation after their formation, or where the primary remanent magnetization is masked by a dominant present-field overprint. For instance, Miocene basalts of the Columbia River Plateau have undergone folding and rotations [e.g., *Reidel et al.*,

1989] and may violate this assumption. Note however that the assumption is justified for the lower continental crust since several studies suggested that the principal source of magnetization is induced magnetization carried by multidomain low-titanium titanomagnetites [e.g., *Shive et al.*, 1992]. Some artifacts may also arise because of the character of aeromagnetic data. First, the data do not consist of a single data set but of a compilation of different surveys with different specifications. Second, aeromagnetic data, especially from older surveys pre-1980, are often not truly measured on a horizontal plane. Instead, surveys were acquired at various elevations and downward or upward continued to a draped surface at a constant elevation above the ground. Despite these various caveats, theoretical curves predicted by a single layer of fractal random magnetization reproduces quite well the power spectra obtained from aeromagnetic data (Figure 3b) indicating that this relatively simple model is appropriate to characterize crustal magnetization.

5.4. Origins and Implications of Individual Features in z_b

[38] Our method is able to delineate robust long-wavelength features associated with spatial variations in the thermal and geologic structure of the crust. However, determining the exact origin of these features requires a careful inspection of the data quality and a comparison with independent geologic and geophysical data. In addition, this method provides information on the relative variations of the depth to the Curie temperature isotherm rather than on their absolute values. We now discuss the origin of a few individual prominent features in the map of z_b that are not observed in the map of heat flow and that may provide new insight into the thermal and geologic structure of the western United States (see also Table 2).

[39] The prominent feature over the western Great Basin (feature 2, Figure 11) characterized by very shallow z_b is not observed in the crustal temperature map derived from heat flow data (Figure 12c). Heat flow is not well constrained in this region, however, because of groundwater circulations, as evidenced in the Eureka Low heat flow area [*Sass et al.*, 1971] (see Figure 1). High heat flow is expected in the Great Basin because of its young magmatic and tectonic history associated with Basin and Range extension ($\sim17–0$ Ma). The shallow z_b feature here also suggests a strong asymmetry in the Great Basin with a much higher heat flow beneath its western part. Higher heat flow over the western Great Basin is supported by the alternative heat flow map of the United States [*Sass et al.*, 1981] derived from the empirical relationship between groundwater silica concentration and heat flow [e.g., *Swanberg and Morgan*, 1978]. This is also consistent with the larger seismicity and contemporary extension observed over this region [e.g., *Bennett et al.*, 2003; *Hammond and Thatcher*, 2004], and in particular within the Central Nevada Seismic Zone and Walker Lane Belt (Figure 12f), a deformation zone accommodating stresses due to Pacific-North American Plate interactions [e.g., *Stewart*, 1988]. If the western Great Basin is indeed a zone of elevated heat flow, the high heat flow could be a consequence of the recent tectonic and magmatic activity in this area or alternatively facilitate deformations by weakening the crust. Our interpretation is also confirmed by several seismic tomography studies suggesting elevated uppermost mantle temperature beneath the western Great

Basin [e.g., *Goes and van der Lee*, 2002; *Yang et al.*, 2008]. In addition, this region of shallow z_b lies beneath the presumed location of the ancestral Cascade arc active about 21 Ma ago [*Christiansen and Yeats*, 1992] (Figure 12f) and the North Nevada Rift, a series of mafic dikes associated with the inception of the Yellowstone hot spot about 17 Ma ago [e.g., *Glen and Ponce*, 2002] (Figure 12f). These magmatic events are likely too old to have an effect on the current distribution of heat flow. However, the shallow bottom of magnetic sources also could be an artifact of the effects on the fractal parameter β of igneous rocks associated with the ancient Cascade arc or with the Northern Nevada Rift or of the tectonic fabric associated to deformation in the Walker Lane Belt.

[40] The shallow z_b over the center of the Colorado Plateau (feature 6, Figure 11) is not observed in the crustal temperature map derived from heat flow data (Figure 12c), which instead shows low temperature values. Distribution of heat flow over the Colorado Plateau is not well constrained, however, because of the scarcity of data. Although tectonically stable since Precambrian times [e.g., *Morgan and Swanberg*, 1985], the Colorado Plateau has been affected by several Cenozoic magmatic events. This shallow z_b feature lies, in particular, beneath the Navajo ($\sim$20–30 Ma) [e.g., *Riter and Smith*, 1996] and Hopi Buttes ($\sim$2–5 Ma) [e.g., *Naeser*, 1971] volcanic fields. Causes of this magmatic activity may be melting of hydrated mantle associated with Farallon plate subduction [e.g., *Smith et al.*, 2004] along a zone of weakness associated with the suture between two Proterozoic terrains [*Karlstrom and Humphreys*, 1998]. A recent seismic experiment [*Gao et al.*, 2004] indicates relatively low seismic velocities beneath the Navajo volcanic field and suggests that this area is also characterized by elevated uppermost mantle temperatures possibly due to mantle upwelling associated with the remnant Farallon slab. This interpretation is consistent with the existence of higher heat flow beneath this area.

[41] Features 9 and 10 (Figure 11) within the Great Plains characterized by shallower z_b are not observed in the crustal temperatures map (Figure 12c) that shows low to medium values. The Great Plains, which form the western edge of the stable North American craton, are principally covered by sedimentary rocks and have not undergone significant deformation since Precambrian time. These two features coincide approximately with the location of Tertiary plutons and volcanic rocks [e.g., *Stewart and Carlson*, 1978] and might be due to effects on the fractal parameter β associated with buried igneous rocks or of tectonic structures within the underlying Proterozoic basement [e.g., *Sims et al.*, 2008].

6. Conclusions and Perspectives

[42] We have improved the method initially developed by *Maus et al.* [1997] for estimating the depth to the bottom of magnetic sources from aeromagnetic data and applied it to aeromagnetic compilations from the western United States. Like earlier methods, this method is based on the spectral analysis of aeromagnetic anomalies. This methodology improves on early studies, however, by incorporating more realistic models of crustal magnetization. Whereas early methods assumed layers with random magnetization and flat power spectra [e.g., *Connard et al.*, 1983; *Blakely*, 1988;

Tanaka et al., 1999; *Ross et al.*, 2006], this method assumes a fractal distribution of magnetization, as proposed by *Maus et al.* [1997].

[43] Shapes of radial power spectra predicted by a model of fractal random magnetization are compatible with radial power spectra obtained from aeromagnetic data in the western United States. Early methods relied on ascertaining the precise wave number of the dominant peak of the spectrum at low wave numbers, often difficult to determine in practice. The method described here does not assume a priori the existence of such a peak but rather uses a broader part of the spectrum. Potentially, this method can be used to estimate three independent parameters of the model: the fractal parameter β of the magnetization and the depth to the top z_t and bottom z_b of the source layer. In practice, it is necessary to specify at least one of the three parameters in order to obtain accurate estimates of the other two unknown parameters. We also observed that the accuracy of the estimation of z_b increases when the size of the window W, used for the calculation of the power spectrum, increases. In particular, for a fractal parameter $\beta = 3$, we may expect a relative error smaller than 25% when $W \geq 15\ z_b$.

[44] The application of this method to the western United States, assuming constant β, allowed us to detect robust long-wavelength variations in the depth to the bottom of magnetic sources z_b. These variations were obtained independent of other parameters, such as β and W. They were also observed using two different aeromagnetic compilations, Nevada and North America. Although the absolute values estimated for z_b are generally too shallow compared to the expected depths to the Curie temperature isotherm, several patterns in z_b correlate with robust heat flow features, suggesting that z_b reflects broad relative variations in heat flow. We also observe correlations of the map of z_b with the distribution of volcanic rocks. Long-wavelength variations in z_b may have different origins: variations of the depth to the bottom of magnetic sources z_b (corresponding to the Curie temperature isotherm, in high heat flow areas, to the base of the crust, in low heat flow areas or to the base of highly magnetized young volcanic rocks in volcanic provinces) or artifacts due to variations of the fractal parameter β (reflecting, instead, variations in the geology). A careful inspection of independent geophysical and geologic data is necessary to determine the exact origin of these features. Because this method requires computing the power spectrum of magnetic anomalies over a large window, it provides only a smoothed image of the variations of the depth to the bottom of magnetic sources that is not expected to be directly correlated to superficial variations of heat flow but instead brings complementary information on deep crustal structures.

[45] The application of this method to aeromagnetic data in the western United States raises three major future directions of improvement. First, our results might be biased in some cases by the quality of the data in the aeromagnetic compilation. Results could be improved using a compilation that better represents long-wavelength anomalies over $\sim$100 km and composed of surveys acquired with homogenous specifications (flight line spacing and elevation). Such improvements in the aeromagnetic compilation could be obtained by including new global data such as low-altitude satellite or high-altitude aeromagnetic surveys covering

broad areas [e.g., *Ravat et al.*, 2008]. Second, our application required an a priori value for the fractal parameter β. We have few constrains on what this parameter should be, however, and we assumed a constant value over the entire study area. Our method would provide better results if we allow spatial variations of the fractal parameter β to better account for geology. Third, our method might be improved by the introduction of independent constraints on the values of z_t and β. Gravity, seismic and drill holes data may, for instance, provide estimates of the depth to the basement in sedimentary basins, therefore providing a minimum depth to the top of magnetic sources z_t. Geology could be used as a guide to constrain the fractal parameter β. Such an exercise is not trivial, since the fractal parameter valid for surface geology might not be representative of the rocks located in the deep crust.

[46] In the future, the application of this method to other areas may provide information on the thermal and geologic structure of the crust and help recognize prospective regions for geothermal exploration. The recent World Digital Magnetic Anomaly Map [*Korhonen et al.*, 2007] may be a suitable database for such studies but will require careful inspection of independent geophysical and geologic data and of the quality of the magnetic data. Finally, a better knowledge of the crustal and uppermost mantle geothermal condition may be obtained by combining heat flow data, depth to the Curie temperature isotherm estimates from magnetic data, and also other indirect temperature indicators, such as depth to the brittle/ductile transition zone from the depth distribution of seismic events [e.g., *Sibson*, 1982; *Chen and Molnar*, 1983; *Scholz*, 1988] and uppermost mantle seismic velocities from tomographic studies.

Appendix A: Evaluation of the Integral Term in the Expression of the Radial Power Spectrum in Equation (3)

[47] In this appendix, we resolve analytically the following integral:

$$I = \int_0^\infty \left(\cosh(k_H \Delta z) - \cos(k_z \Delta z)\right)\left(1 + \left(\frac{k_z}{k_H}\right)^2\right)^{-1-\frac{\beta}{2}} dk_z$$
(A1)

This integral can be expressed as the sum of two integrals. After the following substitution, $x = \frac{k_z}{k_H}$, this integral becomes

$$I = k_H\left[\cosh(k_H\Delta z)\int_0^\infty \left(1+x^2\right)^{-1-\frac{\beta}{2}}dx \right.$$
$$\left. - \int_0^\infty \cos(k_H\Delta z x)\left(1+x^2\right)^{-1-\frac{\beta}{2}}dx\right]$$
(A2)

In this expression, the first integral can be expressed using the gamma function $\Gamma(u)$ (see formula 4 of 3.241 on page 292 of *Gradshteyn and Ryzhik* [1980] with $\mu = 1$, $\nu = 2$, $p = 1$, $q = 1$ and $n = \frac{\beta}{2}$):

$$\int_0^\infty \left(1+x^2\right)^{-1-\frac{\beta}{2}}dx = \frac{\sqrt{\pi}}{2}\frac{\Gamma\left(\frac{1+\beta}{2}\right)}{\Gamma\left(1+\frac{\beta}{2}\right)}$$
(A3)

The second integral can be expressed using the gamma function $\Gamma(u)$ and the modified Bessel function of the second kind $K_\alpha(u)$ (see formula 2 of 3.771, page 426 of *Gradshteyn and Ryzhik* [1980] with $a = k_H\Delta z$, $\beta = 1$ and $\nu = -\frac{1+\beta}{2}$):

$$\int_0^\infty \left(1+x^2\right)^{-1-\frac{\beta}{2}}\cos(k_H\Delta z x)dx = \frac{1}{\sqrt{\pi}}\left(\frac{k_H\Delta z}{2}\right)^{\frac{1+\beta}{2}}$$
$$\cdot \cos\left(\pi\frac{1+\beta}{2}\right)\Gamma\left(-\frac{\beta}{2}\right)K_{\frac{1+\beta}{2}}(k_H\Delta z)$$
(A4)

which becomes (using formula 2 of 8.334, page 937 of *Gradshteyn and Ryzhik* [1980] with $x = \frac{1+\beta}{2}$)

$$\int_0^\infty \left(1+x^2\right)^{-1-\frac{\beta}{2}}\cos(k_H\Delta z x)dx = \sqrt{\pi}\left(\frac{k_H\Delta z}{2}\right)^{\frac{\beta+1}{2}}\frac{K_{\frac{1+\beta}{2}}(k_H\Delta z)}{\Gamma\left(1+\frac{\beta}{2}\right)}$$
(A5)

The integral I therefore becomes

$$I = \frac{\sqrt{\pi}k_H}{\Gamma\left(1+\frac{\beta}{2}\right)}\left(\frac{\cosh(k_H\Delta z)}{2}\Gamma\left(\frac{1+\beta}{2}\right) - K_{\frac{1+\beta}{2}}(k_H\Delta z)\left(\frac{k_H\Delta z}{2}\right)^{\frac{1+\beta}{2}}\right)$$
(A6)

References

Bennett, R. A., B. P. Wernicke, N. A. Niemi, A. M. Friedrich, and J. L. Davis (2003), Contemporary strain rates in the northern Basin and Range province from GPS data, *Tectonics*, 22(2), 1008, doi:10.1029/2001TC001355.

Benz, H. M., R. B. Smith, and W. D. Mooney (1990), Crustal structure of the northwestern Basin and Range province from the 1986 Program for Array Seismic Studies of the Continental Lithosphere seismic experiment, *J. Geophys. Res.*, 95, 21,823–21,842, doi:10.1029/JB095iB13p21823.

Blackwell, D. D. (1983), Heat flow in the northern Basin and Range province, in *The Role of Heat in the Development of Energy and Mineral Resources in the Northern Basin and Range Province*, edited by Geothermal Resources Council, *Spec. Rep.*, 13, 81–93.

Blackwell, D. D. (1989), Regional implications of heat flow of the Snake River Plain, northwestern United States, *Tectonophysics*, 164, 323–343, doi:10.1016/0040-1951(89)90025-5.

Blackwell, D. D., and M. Richards (2004), Geothermal map of North America, 1 sheet, scale 1:6,500,000, Am. Assoc. Pet. Geol., Tulsa, Okla.

Blackwell, D. D., R. G. Bowen, D. A. Hull, J. Riccio, and J. L. Steele (1982), Heat flow, arc volcanism, and subduction in northern Oregon, *J. Geophys. Res.*, 87, 8735–8754, doi:10.1029/JB087iB10p08735.

Blackwell, D. D., J. L. Steele, M. K. Frohme, C. F. Murphey, G. R. Priest, and G. L. Black (1990), Heat flow in the Oregon Cascade Range and its correlation with regional gravity, Curie point depth, and geology, *J. Geophys. Res.*, 95, 19,475–19,493, doi:10.1029/JB095iB12p19475.

Blackwell, D. D., P. T. Negraru, and M. Richards (2007), Assessment of the enhanced geothermal system resource base of the United States, *Nat. Resour. Res.*, 15, 283–308, doi:10.1007/s11053-007-9028-7.

Blakely, R. J. (1988), Curie temperature isotherm analysis and tectonic implications of aeromagnetic data from Nevada, *J. Geophys. Res.*, *93*, 11,817–11,832, doi:10.1029/JB093iB10p11817.

Blakely, R. J. (1995), *Potential Theory in Gravity and Magnetic Applications*, Cambridge Univ. Press, Cambridge, U. K.

Bodell, J. M., and D. S. Chapman (1982), Heat flow in the north-central Colorado Plateau, *J. Geophys. Res.*, *87*, 2869–2884, doi:10.1029/JB087iB04p02869.

Braile, L. W., R. B. Smith, J. Ansorge, M. R. Baker, M. A. Sparlin, C. Prodehl, M. M. Schilly, J. H. Healy, S. Mueller, and K. H. Olsen (1982), The Yellowstone-Snake River Plain seismic profiling experiment: Crustal structure of the eastern Snake River Plain, *J. Geophys. Res.*, *87*, 2597–2609, doi:10.1029/JB087iB04p02597.

Camp, V. E., and M. E. Ross (2004), Mantle dynamics and genesis of mafic magmatism in the intermontane Pacific northwest, *J. Geophys. Res.*, *109*, B08204, doi:10.1029/2003JB002838.

Chen, W. P., and P. Molnar (1983), The depth distribution of intracontinental and intraplate earthquakes and its implications for the thermal and mechanical properties of the lithosphere, *J. Geophys. Res.*, *88*, 4183–4214, doi:10.1029/JB088iB05p04183.

Christiansen, R. L., and R. S. Yeats (1992), Post-Laramide geology of the U.S. Cordilleran region, in *The Geology of North America*, vol. G-3, pp. 350–357, Geol. Soc. Am., Boulder, Colo.

Chulick, G. S., and W. D. Mooney (2002), Seismic structure of the crust and uppermost mantle of North America and adjacent oceanic basins: A synthesis, *Bull. Seismol. Soc. Am.*, *92*, 2478–2492, doi:10.1785/0120010188.

Connard, G., R. Couch, and M. Gemperle (1983), Analysis of aeromagnetic measurements from the Cascade Range in central Oregon, *Geophysics*, *48*, 376–390, doi:10.1190/1.1441476.

Dunlop, D. J., and Ö. Özdemir (1997), *Rock Magnetism: Fundamentals and Frontiers*, 573 pp., Cambridge Univ. Press, New York.

Fedi, M., T. Quarta, and A. De Santis (1997), Inherent power law behavior of magnetic field power spectra from a Spector and Grant ensemble, *Geophysics*, *62*, 1143–1150, doi:10.1190/1.1444215.

Fenneman, N. M., and D. W. Johnson (1946), Physical divisions of the United States, *U.S. Geol. Surv. Spec. Map*, scale 1:7,000,000, Washington, D. C.

Fliedner, M. M., S. L. Klemperer, and N. I. Christensen (2000), Three-dimensional seismic model of the Sierra Nevada Arc, California, and its implications for crustal and upper mantle composition, *J. Geophys. Res.*, *105*, 10,899–10,921, doi:10.1029/2000JB900029.

Frost, B. R., and P. N. Shive (1986), Magnetic mineralogy of the lower continental crust, *J. Geophys. Res.*, *91*, 6513–6521, doi:10.1029/JB091iB06p06513.

Gao, W., S. P. Grand, W. S. Baldridge, D. Wilson, M. West, J. F. Ni, and R. Aster (2004), Upper mantle convection beneath the central Rio Grande Rift imaged by P and S wave tomography, *J. Geophys. Res.*, *109*, B03305, doi:10.1029/2003JB002743.

Gettings, M. E. (2005), Multifractal magnetic susceptibility distribution models of hydrothermally altered rocks in the Needle Creek Igneous Center of the Absaroka Mountains, Wyoming, *Nonlinear Processes Geophys.*, *12*, 587–601.

Glen, J. M. G., and D. A. Ponce (2002), Large-scale fractures related to inception of the Yellowstone hotspot, *Geology*, *30*, 647–650, doi:10.1130/0091-7613(2002)030<0647:LSFRTI>2.0.CO;2.

Glen, J. M. G., E. H. McKee, S. Ludigton, D. A. Ponce, T. G. Hildenbrand, and M. J. Hopkins (2004), Geophysical terranes of the Great Basin and parts of surrounding provinces, *U.S. Geol. Surv. Open File Rep. 2004–1008* (Available at http://pubs.usgs.gov/of/2004/1008/).

Godfrey, N. J., B. C. Beaudoin, S. L. Klemperer, A. Levander, J. Luetgert, A. Meltzer, W. Mooney, and A. Trehu (1997), Ophiolitic basement to the Great Valley forearc basin, California, from seismic and gravity data; implications for crustal growth at the North American continental margin, *Geol. Soc. Am. Bull.*, *109*, 1536–1562, doi:10.1130/0016-7606(1997)109<1536:OBTTGV>2.3.CO;2.

Goes, S., and S. van der Lee (2002), Thermal structure of the North American uppermost mantle inferred from seismic tomography, *J. Geophys. Res.*, *107*(B3), 2050, doi:10.1029/2000JB000049.

Gradshteyn, I. S., and I. M. Ryzhik (1980), *Tables of Integrals, Series, and Products*, 4th ed., Academic, San Diego, Calif.

Gregotski, M. E., O. Jensen, and J. Arkani-Hamed (1991), Fractal stochastic modeling of aeromagnetic data, *Geophysics*, *56*, 1706–1715, doi:10.1190/1.1442983.

Hammond, W., and W. Thatcher (2004), Contemporary tectonic deformation of the Basin and Range province, western United States: 10 years of observation with the Global Positioning System, *J. Geophys. Res.*, *109*, B08403, doi:10.1029/2003JB002746.

Heimgartner, M., J. N. Louie, J. B. Scott, W. Thelen, C. T. Lopez, and M. Coolbaugh (2006), The crustal thickness of the Great Basin: Using seismic refraction to assess regional geothermal potential, *Trans. Geotherm. Resour. Counc.*, *30*, 83–86.

Hunt, C. P., B. M. Moskowitz, and S. K. Banerjee (1995), Magnetic properties of rocks and minerals, in *Rock Physics and Phase Relations: A Handbook of Physical Constants*, edited by T. J. Ahrens, pp. 189–204, AGU, Washington, D. C.

Karlstrom, K. E., and E. D. Humphreys (1998), Persistent influence of Proterozoic accretionary boundaries in the tectonic evolution of southwestern North America: Interaction of cratonic grain and mantle modification events, *Rocky Mt. Geol.*, *33*, 161–179.

Kletetschka, G., P. J. Wasilewski, and P. T. Taylor (2002), The role of hematite–ilmenite solid solution in the production of magnetic anomalies in ground- and satellite-based data, *Tectonophysics*, *347*, 167–177, doi:10.1016/S0040-1951(01)00243-8.

Korhonen, J. V., et al. (2007), *Magnetic Anomaly Map of the World*, Comm. for the Geol. Map of the World, Paris.

Kucks, R. P., P. L. Hill, and D. A. Ponce (2006), Nevada magnetic and gravity maps and data: A website for the distribution of data, *U.S. Geol. Surv. Data Ser.*, *234* (Available at http://pubs.usgs.gov/ds/2006/234).

Lachenbruch, A. H. (1978), Heat flow in the Basin and Range province and thermal effects of tectonic extension, *Pure Appl. Geophys.*, *117*, 34–50, doi:10.1007/BF00879732.

Lachenbruch, A. H., and J. H. Sass (1977), Heat flow in the United States and the thermal regime of the crust, in *The Earth's Crust its Nature and Physical Properties*, *Geophys. Monogr. Ser.*, vol. 20, edited by J. G. Heacock et al., pp. 626–675, AGU, Washington, D. C.

Lachenbruch, A. H., and J. H. Sass (1978), Models of an extending lithosphere and heat flow in the Basin and Range province, *Mem. Geol. Soc. Am.*, *152*, 209–250.

Leaver, D. S., W. D. Mooney, and W. M. Kohler (1984), A refraction study of the Oregon Cascades, *J. Geophys. Res.*, *89*, 3121–3134, doi:10.1029/JB089iB05p03121.

Leonardi, S., and H.-J. Kümpel (1996), Scaling behaviour of vertical magnetic susceptibility and its fractal characterization: An example from the German Continental Deep Drilling Project (KTB), *Geol. Rundsch.*, *85*, 50–57, doi:10.1007/s005310050051.

Lesur, V., and S. Maus (2006), A global lithospheric magnetic field model with reduced noise level in the polar regions, *Geophys. Res. Lett.*, *33*, L13304, doi:10.1029/2006GL025826.

Lovejoy, S., S. Pecknold, and D. Schertzer (2001), Stratified multifractal magnetization and surface geomagnetic fields-I. Spectral analysis and modelling, *Geophys. J. Int.*, *145*, 112–126, doi:10.1111/j.1365-246X.2001.00344.x.

Maus, S., and V. P. Dimri (1994), Scaling properties of potential fields due to scaling sources, *Geophys. Res. Lett.*, *21*, 891–894, doi:10.1029/94GL00771.

Maus, S., and V. P. Dimri (1995), Potential field power spectrum inversion for scaling geology, *J. Geophys. Res.*, *100*, 12,605–12,616, doi:10.1029/95JB00758.

Maus, S., and V. P. Dimri (1996), Depth estimation from the scaling power spectrum of potential fields?, *Geophys. J. Int.*, *124*, 113–120, doi:10.1111/j.1365-246X.1996.tb06356.x.

Maus, S., D. Gordon, and D. Fairhead (1997), Curie temperature depth estimation using a self-similar magnetization model, *Geophys. J. Int.*, *129*, 163–168, doi:10.1111/j.1365-246X.1997.tb00945.x.

Maus, S., M. Rother, R. Holme, H. Luhr, N. Olsen, and V. Haak (2002), First scalar magnetic anomaly map from CHAMP satellite data indicates weak lithospheric field, *Geophys. Res. Lett.*, *29*(14), 1702, doi:10.1029/2001GL013685.

McEnroe, S. A., F. Langenhorst, P. Robinson, G. D. Bromiley, and C. S. J. Shaw (2004), What is magnetic in the lower crust?, *Earth Planet. Sci. Lett.*, *226*, 175–192, doi:10.1016/j.epsl.2004.07.020.

Morgan, P., and C. A. Swanberg (1985), On the Cenozoic uplift and tectonic stability of the Colorado Plateau, *J. Geodyn.*, *3*, 39–63, doi:10.1016/0264-3707(85)90021-3.

Naeser, C. W. (1971), Geochronology of the Navajo-Hopi diatremes, Four Corners area, *J. Geophys. Res.*, *76*, 4978–4985, doi:10.1029/JB076i020p01978.

North American Magnetic Anomaly Group (NAMAG) (2002), Digital data grids for the magnetic anomaly map of North America, *U.S. Geol. Surv. Open File Rep. 02–414*, (Available at http://pubs.usgs.gov/of/2002/ofr-02-414/).

Okubo, Y., R. J. Graf, R. O. Hansen, K. Ogawa, and H. Tsu (1985), Curie point depths of the island of Kyushu and surrounding areas, Japan, *Geophysics*, *50*, 481–494, doi:10.1190/1.1441926.

Parsons, T., J. McCarthy, W. M. Kohler, C. J. Ammon, H. M. Benz, J. A. Hole, and E. E. Criley (1996), Crustal structure of the Colorado Plateau, Arizona: Application of new long-offset seismic data analysis techniques, *J. Geophys. Res.*, *101*, 11,173–11,194, doi:10.1029/95JB03742.

Pecknold, S., S. Lovejoy, and D. Schertzer (2001), Stratified multifractal magnetization and surface geomagnetic fields-II. Multifractal analysis and simulations, *Geophys. J. Int.*, 145, 127–144, doi:10.1111/j.1365-246X.2001.00345.x.

Peng, X., and E. D. Humphreys (1998), Crustal velocity structure across the eastern Snake River Plain and the Yellowstone swell, *J. Geophys. Res.*, 103, 7171–7186, doi:10.1029/97JB03615.

Pilkington, M., and J. P. Todoeschuck (1993), Fractal magnetization of continental crust, *Geophys. Res. Lett.*, 20, 627–630, doi:10.1029/92GL03009.

Pilkington, M., and J. P. Todoeschuck (1995), Scaling nature of crustal susceptbilities, *Geophys. Res. Lett.*, 22, 779–782, doi:10.1029/95GL00486.

Pilkington, M., J. P. Todoeschuck, and M. E. Gregotski (1994), Using fractal crustal magnetization models in magnetic interpretation, *Geophys. Prospect.*, 42, 677–692, doi:10.1111/j.1365-2478.1994.tb00235.x.

Ravat, D., A. Pignatelli, I. Nicolosi, and M. Chiappini (2007), A study of spectral methods of estimating the depth to the bottom of magnetic sources from near-surface magnetic anomaly data, *Geophys. J. Int.*, 169, 421–434, doi:10.1111/j.1365-246X.2007.03305.x.

Ravat, D., T. Sabaka, A. Elshayat, A. Aref, E. Elawadi, R. Kucks, P. Hill, J. Phillips, C. Finn, C. Bouligand, and R. J. Blakely (2008), A preliminary full spectrum magnetic anomaly database of the United States with improved long wavelengths for studying continental dynamics, *Eos Trans. AGU*, 89(53), Fall Meet. Suppl., Abstract GP52A–02.

Reidel, S. P., K. R. Fecht, M. C. Hagwood, and T. L. Tolan (1989), The geologic evolution of the central Columbia Plateau, in *Volcanism and Tectonism in the Columbia River Flood-Basalt Province*, edited by S. P. Reidel and P. R. Hooper, *Spec. Pap. Geol. Soc. Am.*, 239, 247–264.

Riter, J. C. A., and D. Smith (1996), Xenolith constraints on the thermal history of the mantle below the Colorado Plateau, *Geology*, 24, 267–270, doi:10.1130/0091-7613(1996)024<0267:XCOTTH>2.3.CO;2.

Ross, H. E., R. J. Blakely, and M. D. Zoback (2006), Testing the use of aeromagnetic data for the determination of Curie depth in California, *Geophysics*, 71, L51, doi:10.1190/1.2335572.

Sass, J. H., A. H. Lachenbruch, R. J. Munroe, G. W. Green, and T. H. Moses Jr. (1971), Heat flow in the western United States, *J. Geophys. Res.*, 76, 6356–6431.

Sass, J. H., D. D. Blackwell, D. S. Chapman, J. K. Costain, E. R. Decker, L. A. Lawver, and C. A. Swanberg (1981), Heat flow of the crust of the United States, in *Physical Properties of Rocks and Minerals*, edited by Y. S. Touloukian, W. R. Judd, and R. F. Roy, pp. 503–548, McGraw-Hill, New York.

Sass, J. H., A. H. Lachenbruch, S. P. Galanis, P. Morgan, S. S. Priest, T. H. Moses, and R. J. Munroe (1994), Thermal regime of the southern Basin and Range province: 1. Heat flow data from Arizona and the Mojave Desert of California and Nevada, *J. Geophys. Res.*, 99, 22,093–22,119, doi:10.1029/94JB01891.

Scholz, C. H. (1988), The brittle-plastic transition and the depth of seismic faulting, *Geol. Rundsch.*, 77, 319–328, doi:10.1007/BF01848693.

Schruben, P. G., R. E. Arndt, and W. J. Bawiec (1998), Geology of the conterminous United States at 1:2,500,000 scale: A digital representation of the 1974 P. B. King and H. M. Beikman map, *U.S. Geol. Surv. Digital Data Ser.*, 11, (Available at http://pubs.usgs.gov/dds/dds11/).

Schultz, A. P., and R. S. Crosson (1996), Seismic velocity structure across the central Washington Cascade Range from refraction interpretation with earthquake sources, *J. Geophys. Res.*, 101, 27,899–27,916, doi:10.1029/96JB02289.

Shive, P. N., R. J. Blakely, B. R. Frost, and D. M. Fountain (1992), Magnetic properties of the lower continental crust, in *Continental Lower Crust*, edited by D. M. Fountain et al., pp. 145–177, Elsevier Sci., New York.

Sibson, R. H. (1982), Fault zone models, heat flow, and the depth distribution of earthquakes in the continental crust of the United States, *Bull. Seismol. Soc. Am.*, 72, 151–163.

Sims, P. K., R. W. Saltus, and E. D. Anderson (2008), Precambrian basement structure map of the continental United States: An interpretation of geologic and aeromagnetic data, *U.S. Geol. Surv. Sci. Invest. Map*, 3012.

Smith, D., J. N. Connelly, K. Manser, D. E. Moser, T. B. Housh, F. W. McDowell, and L. E. Mack (2004), Evolution of Navajo eclogites and hydration of the mantle wedge below the Colorado Plateau, southwestern United States, *Geochem. Geophys. Geosyst.*, 5, Q04005, doi:10.1029/2003GC000675.

Spector, A., and S. Grant (1970), Statistical models for interpreting aeromagnetic data, *Geophysics*, 35, 293–302, doi:10.1190/1.1440092.

Stewart, J. H. (1988), Tectonics of the Walker Lane belt, western Great Basin: Mesozoic and Cenozoic deformation in a zone of shear, in *The Geotectonic Development of California: Englewood Cliffs*, edited by W. G. Ernst, pp. 71–86, Prentice-Hall, Englewood Cliffs, N. J.

Stewart, J. H., and J. E. Carlson (1978), Generalized maps showing distribution, lithology, and age of Cenozoic igneous rocks in the western United States, in *Cenozoic Tectonics and Regional Geophysics of the Western Cordillera*, edited by R. B. Smith and G. P. Eaton, pp. 263–264, *Mem. Geol. Soc. Am.*, 152, Boulder, Colo.

Swanberg, C. A., and P. Morgan (1978), The linear relation between temperatures based on the silica content of groundwater and regional heat flow: A new heat flow map of the United States, *Pure Appl. Geophys.*, 117, 227–241, doi:10.1007/BF00879749.

Tanaka, A., Y. Okubo, and O. Matsubayashi (1999), Curie point depth based on spectrum analysis of the magnetic anomaly data in East and Southeast Asia, *Tectonophysics*, 306, 461–470, doi:10.1016/S0040-1951(99)00072-4.

Wasilewski, P. J., and M. A. Mayhew (1992), The Moho as a magnetic boundary revisited, *Geophys. Res. Lett.*, 19, 2259–2262, doi:10.1029/92GL01997.

Wolf, L., and J. J. Cipar (1993), Through thick and thin: A new model for the Colorado Plateau from seismic refraction data from Pacific to Arizona crustal experiment, *J. Geophys. Res.*, 98, 19,881–19,894, doi:10.1029/93JB02163.

Yang, Y., M. H. Ritzwoller, F.-C. Lin, and M. P. Moschetti (2008), Structure of the crust and uppermost mantle beneath the western United States revealed by ambient noise and earthquake tomography, *J. Geophys. Res.*, 113, B12310, doi:10.1029/2008JB005833.

_____

R. J. Blakely and J. M. G. Glen, U.S. Geological Survey, MS989, 345 Middlefield Rd., Menlo Park, CA 94025, USA.

C. Bouligand, Laboratoire de Géophysique Interne et Tectonophysique, Université Joseph-Fourier, CNRS, BP 53, F-38041 Grenoble, CEDEX 9, France. (Claire.Bouligand@obs.ujf-grenoble.fr)